# Photoactivity of amorphous and crystalline $TiO_2$ nanotube arrays (TNA) films in gas phase $CO_2$ reduction to methane with simultaneous $H_2$ production

Santos, Janaina S.; Fereidooni, Mohammad; Márquez, Victor; Paz-López, Christian V.; Villanueva, Martin S.; Buijnsters, Josephus G.; Praserthdam, Supareak; Praserthdam, Piyasan

**DOI**
10.1016/j.envres.2023.117919

**Publication date**
2024

**Document Version**
Final published version

**Published in**
Environmental Research

**Citation (APA)**
Santos, J. S., Fereidooni, M., Márquez, V., Paz-López, C. V., Villanueva, M. S., Buijnsters, J. G., Praserthdam, S., & Praserthdam, P. (2024). Photoactivity of amorphous and crystalline $TiO_2$ nanotube arrays (TNA) films in gas phase $CO_2$ reduction to methane with simultaneous $H_2$ production. *Environmental Research*, *244*, Article 117919. https://doi.org/10.1016/j.envres.2023.117919

Environmental Research 244 (2024) 117919

Contents lists available at ScienceDirect

Environmental Research

journal homepage: www.elsevier.com/locate/envres

# Photoactivity of amorphous and crystalline $TiO_2$ nanotube arrays (TNA) films in gas phase $CO_2$ reduction to methane with simultaneous $H_2$ production

Janaina S. Santos [a], Mohammad Fereidooni [a], Victor Márquez [a], Christian V. Paz-López [a], Martin S. Villanueva [b], Josephus G. Buijnsters [c], Supareak Praserthdam [d], Piyasan Praserthdam [a,*]

[a] Center of Excellence on Catalysis and Catalytic Reaction Engineering (CECC), Department of Chemical Engineering, Faculty of Engineering, Chulalongkorn University, Bangkok, 10330, Thailand
[b] Facultad de Ingeniería, Benemerita Universidad Autonoma de Puebla, Apartado Postal J-39, CP, 72570, Puebla, Mexico
[c] Department of Precision and Microsystems Engineering, Research Group of Micro and Nano Engineering, Delft University of Technology, Mekelweg 2, 2628 CD, Delft, the Netherlands
[d] High-Performance Computing Unit, Center of Excellence on Catalysis and Catalytic Reaction Engineering (CECC-HCU), Department of Chemical Engineering, Faculty of Engineering, Chulalongkorn University, Bangkok, 10330, Thailand

ARTICLE INFO

*Keywords:*
$TiO_2$ nanotubes
$CO_2$ photoreduction
Amorphous titania
Anatase
Methane
Hydrogen generation

ABSTRACT

This study assessed the photoactivity of amorphous and crystalline $TiO_2$ nanotube arrays (TNA) films in gas phase $CO_2$ reduction. The TNA photocatalysts were fabricated by titanium anodization and submitted to an annealing treatment for crystallization and/or cathodic reduction to introduce $Ti^{3+}$ and oxygen vacancies into the $TiO_2$ structure. The cathodic reduction demonstrated a significant effect on the generated photocurrent. The photoactivity of the four TNA catalysts in $CO_2$ reduction with water vapor was evaluated under UV irradiation for 3 h, where $CH_4$ and $H_2$ were detected as products. The annealed sample exhibited the best performance towards methane with a production rate of 78 μmol $g_{cat}^{-1}$ $h^{-1}$, followed by the amorphous film, which also exhibited an impressive formation rate of 64 μmol $g_{cat}^{-1}$ $h^{-1}$. The amorphous and reduced-amorphous films exhibited outstanding photoactivity regarding $H_2$ production (142 and 144 μmol $g_{cat}^{-1}$ $h^{-1}$, respectively). The annealed catalyst also revealed a good performance for $H_2$ production (132 μmol $g_{cat}^{-1}$ $h^{-1}$) and high stability up to five reaction cycles. Molecular dynamic simulations demonstrated the changes in the band structure by introducing oxygen vacancies. The topics covered in this study contribute to the Sustainable Development Goals (SDG), involving affordable and clean energy (SDG#7) and industry, innovation, and infrastructure (SDG#9).

## 1. Introduction

This study describes the use of nanostructured oxide photocatalysts in energy conversion and environmental remediation applications. These topics contribute to the Sustainable Development Goals (SDG), involving affordable and clean energy (SDG#7) and industry, innovation, and infrastructure (SDG#9). The emission of greenhouse gases in the atmosphere and its effect on global climate changes is an important environmental problem caused by anthropogenic activities. As a major component of greenhouse gases, greater efforts have been made by the scientific community to develop sustainable processes to capture $CO_2$ and convert it into other value-added chemicals to supply the chemical industry and energy sector. The $CO_2$ reduction reaction can be catalyzed via photo-, electro-, photoelectro-, and thermo-chemical processes forming a plethora of products like CO, $CH_4$, $CH_3OH$, $HCOO^-$, $C_2H_5OH$, and other chemicals (Fan and Tahir, 2022; Fu et al., 2019; Giziński et al., 2020). The formation of a specific product depends on the type of process, catalyst properties, reactor configurations, and reactants composition/phase. Among the processes, photocatalytic $CO_2$ reduction under sunlight is considered the most sustainable strategy. To overcome the low efficiency, the main drawback for large-scale industrial applications, significant attention is being given to the design of novel catalysts

* Corresponding author.
*E-mail address:* piyasan.p@chula.ac.th (P. Praserthdam).

https://doi.org/10.1016/j.envres.2023.117919
Received 20 September 2023; Received in revised form 14 November 2023; Accepted 9 December 2023
Available online 15 December 2023

with specific composition, architecture, and functionalization for an efficient $CO_2$ photoconversion (Sharma et al., 2022).

The high stability, non-toxicity, availability, photocorrosion resistance, suitable band structure, and redox ability turn $TiO_2$ into the most explored photocatalyst in environmental and energy applications (Domínguez-Espíndola et al., 2022; Paz-López et al., 2023). However, the rapid recombination of the photogenerated carriers and low absorption under visible light are still the main drawbacks motivating the development of novel $TiO_2$-based photocatalysts. Currently, the focus of the studies on the photocatalytic activity of $TiO_2$ relies on enhancing its performance, especially under solar light irradiation by doping, surface modification, nanostructuring, heterojunction, and decoration with other materials (Babaie-Aghdam et al., 2023; Goto et al., 2022).

The nanostructured $TiO_2$ films like the $TiO_2$ nanotubes arrays (TNA) films synthesized via anodization technique are widely explored in dye-sensitized solar cells, photo-assisted fuel cells, water treatment, and water splitting for hydrogen generation (Santos et al., 2021). However, its utilization in $CO_2$ photoreduction can be considered relatively new, being developed moderately in the past decade with few and constant numbers of publications, but it has been boosted just after 2020 (Hossen et al., 2022). Still in the development stage, the fundamental aspects, reaction mechanisms, product selectivity, and thermodynamics of TNA in photocatalytic $CO_2$ reduction are not well established, stimulating more studies on the topic.

The most recent studies of gas phase $CO_2$ photoreduction using TNA-based materials explored them in the crystalline form (anatase and anatase/rutile mixtures) (Gao et al., 2020), doped (Qian et al., 2020), modified with noble metals (Khatun et al., 2019; Zeng et al., 2020), combined with carbon-based materials (Rambabu et al., 2019; Zhang et al., 2021a), and forming heterostructures with other semiconductors like $Cu_xO$ (Savchuk et al., 2022) or CdS/ZnS (Cheng et al., 2021). Regarding bare TNA photocatalysts, there are few published studies, mainly focused on the effects of crystallization (Kar et al., 2019) and light irradiation source (Li et al., 2018a; Zhang et al., 2021b) on the $CO_2$ conversion efficiency. Introducing defects like oxygen vacancies was also explored to increase the $TiO_2$ absorption under visible light (Gao et al., 2020).

Despite being considered inactive or inefficient for photocatalytic reactions, recent studies have demonstrated an extraordinary photocatalytic activity of amorphous $TiO_2$ in $CO_2$ photoreduction (Fereidooni et al., 2023b; Kharade and Chang, 2020; Santos et al., 2022). The amorphous titania presents a large number of traps on the surface, like hydroxyl groups, that can reduce the recombination of the charge carriers and increase the electron lifetime. Regarding amorphous TNA, Santos et al. demonstrated the photocatalytic conversion of $CO_2$ to methane with an impressive result of 14.0 μmol $g_{cat}^{-1}$ $h^{-1}$ and high stability up to six reaction cycles for methane production using a bare $TiO_2$ material without any modification procedure (Santos et al., 2022).

The main products of $CO_2$ photoreduction with water using TNA-based materials reported in the literature are $CH_4$, CO, $C_2H_4$, and $C_2H_6$ (Hossen et al., 2022). $H_2$ gas can be detected among the products of $CO_2$ photoreduction when sacrificial agents, like methanol, are added to the water phase (Zhao et al., 2012). The strategy for achieving higher $H_2$ yields is the $TiO_2$ functionalization with another co-catalyst, especially noble metals (Zhao et al., 2012). Usually, the photocatalytic $H_2$ production and $CO_2$ photoreduction are investigated independently in the literature. Herein, we describe for the first time the simultaneous formation of methane and hydrogen from gas phase $CO_2$ reduction reaction by using amorphous and crystalline TNA photocatalysts in a bare form without co-catalysts. The effect of introducing defects like $Ti^{3+}$ and oxygen vacancies by cathodic reduction was evaluated, and molecular dynamic simulations were performed to understand how these defects can alter the band structure of the material. The obtained results are discussed in the view of the potential usage of anodized nanostructured $TiO_2$ films as a base material for photocatalysts in renewable fuel production.

## 2. Materials and methods

### 2.1. TNA fabrication

The TNA catalysts were fabricated by Ti anodization at 50 V for 30 min in ethylene glycol (EG) solution containing 0.75% wt. $NH_4F$ and 10 vol% $H_2O$. After anodization, samples were submitted to two post-treatments: annealing at 450 °C under air for 2 h and/or cathodic reduction at −3 V for 1 min in 0.1 M $NaH_2PO_4$, resulting in a total of four different samples (A, B, C, and D), as illustrated in Figure A1 in Supporting Information (SI file). Since the as-anodized films prepared at voltages up to 60 V are typically amorphous (Santos et al., 2022), for simplification, the samples A and B are denoted as amorphous and rd-amorphous (amorphous/reduced), respectively. Similarly, samples C and D are referred to as annealed and rd-annealed (annealed/reduced).

### 2.2. Material characterization

The morphology and film composition of the TNA samples were analyzed by scanning electron microscopy (SEM) and energy-dispersive X-ray spectroscopy (EDX) using an AMICUS photoelectron spectrometer with an Mg Kα X-ray source controlled by KRATOS VISION2 software at 20 mA and 10 keV. The microstructure was analyzed by X-ray diffraction (XRD) using a Bruker D8 Advance with a Cu anode and Kα1 (1.544 Å) irradiation. The X-ray photoelectron spectroscopy (XPS) analysis was performed using an Axis Supra spectrometer (Kratos®) with Mg Kα X-ray radiation (1253.6 eV) at 10 kV, 20 mA and pass energy of 75 eV. The Raman spectra were acquired using a Horiba XploRA Plus microscope under a laser excitation at 532 nm. The optical properties were analyzed by using a UV–Vis spectrophotometer (Agilent Cary 5000) in the 200 and 800 nm range. The bandgap values were calculated from UV–Vis spectra by applying Tauc's equation (Bharti et al., 2016). The electronic properties were investigated by PL spectroscopy technique using a Horiba 4P-Fluoromax spectrofluorometer with a Xenon lamp as the excitation source and an excitation wavelength of 280 and 320 nm at room temperature.

Mott-Schottky (MS), electrochemical impedance spectroscopy (EIS), and photocurrent experiments were performed in 0.1 M phosphate buffer solution (pH 7.0) purged with $N_2$ or $CO_2$ for 30 min using a Multi Autolab/M204 potentiostat (Metrohm®). A three-electrode configuration cell was used for MS and EIS measurements. A photoelectrochemical cell (R/T/A – Spectro-EC 1.75 mL, Redox.me®) was used for the photocurrent measurements, where the quartz window was irradiated with a 1000 W Xe lamp during the experiments. The electrochemical conditions are described in the SI file.

### 2.3. Photocatalytic $CO_2$ reduction

The photocatalytic $CO_2$ reduction was conducted in a three-way quartz reactor placed inside a box containing six UV lamps (UVC 16 W), as described previously (Santos et al., 2022). The reactor was charged with 100 mL DI water, and the catalyst was held in the headspace of the reactor at 6 cm from the water surface. The system was sealed, and the $CO_2$ gas was injected into the liquid water phase for 30 min and maintained in the dark for another 30 min. Immediately before light irradiation, the gas composition of the vapor flow in the headspace was measured by gas chromatography (GC), and no products were detected. The aliquots were collected every 30 min for 3 h. The concentration of the gaseous products was measured by two GCs, one with a flame ionization detector (GC-FID, Shimadzu, GC-14A) for the exclusive detection of hydrocarbons and the other with a thermal conductivity detector (GC-TCD, Shimadzu, 2014C) for the detection of other gaseous products, like $H_2$, CO, etc. Controlled experiments were carried out to ensure the carbon source is unique from $CO_2$, as described in the SI file. The catalyst stability test was performed using the optimized condition. The $CO_2$ reduction experiment was repeated by five reaction cycles. The

mass of the photocatalysts used in calculating the production concentrations was estimated using the geometric descriptors and morphological parameters extracted from SEM image analysis. See details in the SI file.

### 2.4. Theoretical methods

The theoretical computations were performed by BIOVIA Materials Studio 7.0. The band structure simulations were conducted using the Cambridge Serial Total Energy Package (CASTEP). The amorphous $TiO_2$ structure was constructed from an anatase $TiO_2$ supercell of 48 atoms (Paz et al., 2022), where the top surface was exposed to simulate the interface. For both anatase $TiO_2$ (101) plane and amorphous $TiO_2$ structures, the Perdew-Burke-Ernzerhof (PBE) functional within the generalized gradient approximation (GGA) framework was employed. Ultrasoft pseudopotentials were utilized to describe ion-electron interactions with a plane-wave cut-off energy set at 500 eV. Brillouin zone sampling was achieved using a 4 × 4 × 2 Monkhorst-Pack grid. Convergence criteria were set as follows: a maximum energy difference of $1 \times 10^{-5}$ Ha, a maximum force per atom of 0.002 Ha/Å, and a maximum displacement between iterations of 0.005 Å. The DFT + U method was implemented to refine the bandgap estimation, incorporating Hubbard terms with $U_d = 10.0$ eV and $U_p = 7.0$ eV to improve the accuracy of the bandgap prediction. To prevent interactions between repeating slabs, a 20 Å vacuum was applied in the Z-direction. The creation of oxygen vacancies ($O_v$) was achieved by selectively removing oxygen atoms from the crystal structure.

## 3. Results and discussion

### 3.1. TNA film properties

In this study, four samples were prepared under the same anodizing conditions (50 V, 30 min, EG-F-based electrolyte). The growth of $TiO_2$ nanotubes over the titanium surface under these anodizing conditions was described in previous studies (Santos et al., 2022, 2023b). The anodized samples were submitted to the thermal annealing for crystallization and/or cathodic reduction. This latter procedure was used to

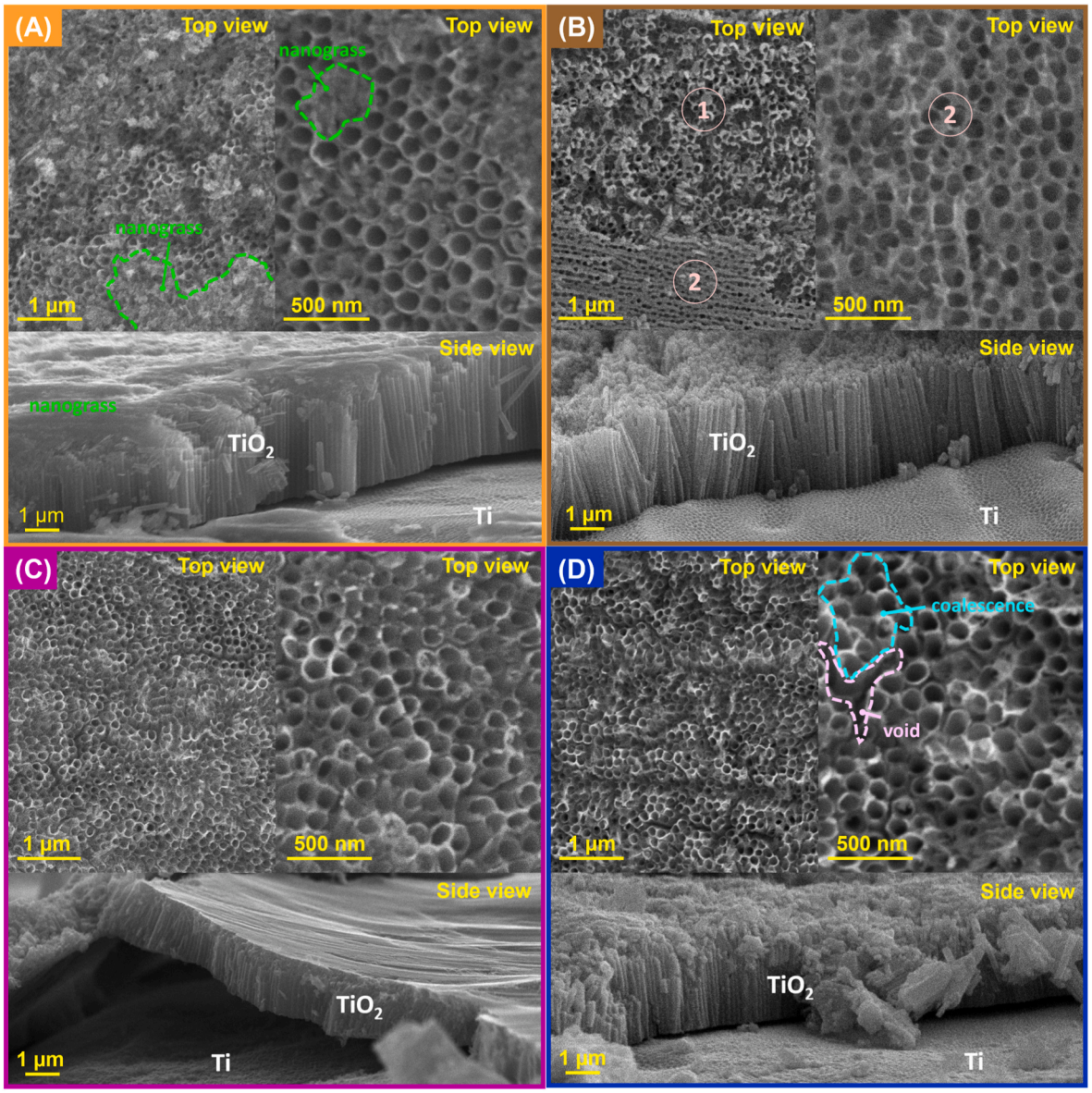


**Fig. 1.** SEM top and side view images of the TNA photocatalysts: (A) as anodized, (B) anodized film after the cathodic reduction, (C) anodized film annealed at 450 °C, and (D) annealed film after the cathodic reduction (D). Regions (1) and (2) in sample B exhibit nanotubular and nanoporous morphology, respectively.

reduce interfacial $Ti^{4+}$ ions to $Ti^{3+}$ and introduce oxygen vacancies into the oxide via a self-doping mechanism (Cheng et al., 2022).

Fig. 1 depicts the top and side view of TNA films obtained by SEM before (A) and after the post-treatments (B, C, and D), characterized by the typical nanotubular structure of the TNA films. However, some differences in the nanotubular morphology were observed depending on the post-treatment type. In sample A, residual oxide on the top of the nanotubes was observed. This structure, namely nanograss, is formed due to the prolonged exposition of fluoride ions, promoting the chemical etching of the oxide tubes (Kim et al., 2008). The amorphous sample modified by the cathodic reduction (sample B) is characterized by the presence of two regions with different morphologies: nanotubular (1) and nanoporous (2). A thin nanoporous layer was observed over some areas on the top surface of the film (sample B), where the gap between nanotubes disappeared. However, the side view suggested that the nanotubular structure remained intact below the nano-thin layer. Similar morphology was observed in $TiO_2$ films anodized at 50 V in both EG- and HF-based electrolytes via a long two-step anodization method (27 h) (Ali et al., 2011). In the annealed samples, no visual changes were observed after the cathodic reduction (from C to D), but the nanograss disappeared after the heat treatment (from A to C).

SEM image analysis demonstrates that the average inner diameter and wall thickness did not significantly change (Figure B1 in SI file). However, the average void among nanotubes increased from the amorphous (sample A) to the annealed films (samples C and D), indicating a slight coalescence of the nanotubes on the top. The nanotube inner diameter presented values in the 80–120 nm range, with an average value of 109 ± 10 nm, 99 ± 10 nm, 96 ± 10 nm, and 99 ± 10 nm for the samples A, B, C and D, respectively. The respective thicknesses of the oxide films, measured at different sites, were 3.3 ± 0.1, 3.1 ± 0.2, 2.2 ± 0.4, and 3.1 ± 0.1 μm. The geometric parameters used to estimate the total mass of the catalyst are shown in the SI file. A shrinkage of ~ 33% in the TNA layer thickness from the as-anodized (A) to the annealed sample (C) was observed, which can be attributed to the dehydration of the $TiO_2$ layer. An increase of ~ 29% in the layer thickness is observed from the annealed (C) to the reduced-annealed sample (D). This behavior can be associated with the TNA rehydration in $NaH_2PO_4$ solution during the cathodic reduction procedure.

Table 1 depicts the compositional analysis of the oxide layer obtained by the semi-quantitative EDX analysis. Ti and O were the major components of the films as expected for $TiO_2$ nanotubes, with Ti content varying from 32 to 37 at.% and O content ranging from 45 to 49 at.%. Despite the slight difference among the samples, the proportion between Ti and O was constant, with a Ti/O ratio of 0.7 (Table C1 in SI file). N, F, and C species from the EG + $NH_4F$ + $H_2O$ electrolyte were incorporated into the film in minor quantities but at different extensions depending on the post-treatment. The most significant variation was in the F and C content; both decreased after the annealing step, indicating a loss by evaporation during the heat treatment. The carbon content is commonly detected in $TiO_2$ materials, not only from residual products of the synthesis but also from air contamination during their manipulation (Santos et al., 2022; Zaleska et al., 2008). Small contents of Na and P (<2.5 at.%) were detected in the samples reduced cathodically in the $NaH_2PO_4$ electrolyte (samples B and D).

**Table 1**
EDX semi-quantitative analysis of the TNA samples anodized in EG solution containing 0.75 wt% $NH_4F$ and 10 vol% $H_2O$ and submitted to annealing and/or cathodic reduction.

| Elements | Sample A/at.% (amorphous) | Sample B/at.% (rd-amorphous) | Sample C/at. % (annealed) | Sample D/at. % (rd-annealed) |
|---|---|---|---|---|
| Ti | 33.4 ± 0.1 | 32.7 ± 0.4 | 36.4 ± 0.6 | 36.7 ± 0.3 |
| O | 46.3 ± 0.5 | 45.9 ± 0.3 | 49.3 ± 0.2 | 49.2 ± 0.2 |
| N | 9.4 ± 0.2 | 7.7 ± 0.1 | 10.9 ± 0.3 | 10.9 ± 0.1 |
| F | 6.0 ± 0.1 | 7.3 ± 0.3 | 1.2 ± 0.1 | 1.0 ± 0.0 |
| C | 4.9 ± 0.4 | 3.9 ± 0.3 | 2.2 ± 0.2 | 1.9 ± 0.2 |
| Na | – | 0.4 ± 0.2 | – | 0.1 ± 0.0 |
| P | – | 2.1 ± 0.0 | – | 0.2 ± 0.0 |
| total | 100.0 | 100.0 | 100.0 | 100.0 |

Fig. 2 depicts the X-ray diffractograms and Raman scattering spectra of the four TNA samples. The X-ray diffractograms of samples A and B confirm that these samples are amorphous, as expected for non-annealed TNA films. In these two samples, only the peaks referring to the titanium substrate were identified. The standard XRD pattern of hexagonal titanium (PDF 00-044-1294) was used as a reference. On the other hand, samples C and D exhibited the diffraction peaks corresponding to anatase, besides the peaks of the metallic Ti substrate. The standard XRD pattern of anatase $TiO_2$ was used as a reference (PDF 01-086-1157) (Sánchez et al., 1996). The main anatase peak (101) was observed at 25.3°, while the other characteristic peaks were observed at 37.9° (004), 48° (200), 54° (105), and 55.1° (211). The average crystallite size calculated by the Debye-Scherrer formula (Gholami et al., 2020) using the anatase main peak (101) was 29.4 nm.

The Raman spectra also confirmed the microstructure of the oxide films (Fig. 2b). The bands observed in the 100-800 $cm^{-1}$ range are related to the bonds in the $TiO_6^{8-}$ octahedra, which are distorted in the amorphous titania and moderately distorted in the anatase phase (Hardcastle et al., 2011). The broad bands centered at 155, 510, and 623 $cm^{-1}$ in the spectra of samples A and B can be attributed to Ti–O bonds from the distorted $TiO_6^{8-}$ octahedra in the amorphous $TiO_2$. The band at 384 $cm^{-1}$ is attributed to the O–O bond in the distorted $TiO_6^{8-}$ octahedra of the amorphous oxide. In the spectra of samples C and D, the high-intensity band observed at 145 $cm^{-1}$ and a shoulder at 200 $cm^{-1}$ are related to the Ti–Ti bond in the slightly distorted $TiO_6^{8-}$ octahedra structure in the anatase. The band centered at 397 $cm^{-1}$ can be credited to the O–O bond, while the bands at 517 and 636 $cm^{-1}$ can be credited to Ti–O bonds in $TiO_6^{8-}$ octahedra in the anatase. The broad bands observed in the 1000-1700 $cm^{-1}$ range and a shoulder around 895 $cm^{-1}$, can be assigned to the Raman active modes of ethylene glycol (Lamberti et al., 2015), the presence of carbonaceous content (Pardanaud et al., 2019), or products of the EG electro-oxidation (Jardak et al., 2017). The absence of these bands in the annealed samples (C and D) suggests the oxidation/evaporation of these species during the heat treatment.

Fig. 3 shows the survey XPS spectra of the synthesized samples and the Ti 2p and O 1s deconvoluted spectra used to identify the oxidation state of the species in the TNA films. The main peaks in the survey spectra correspond to F 1s, O 1s, Ti 2p and C 1s core levels. Besides Ti 2p and O 1s peaks originating from the $TiO_2$ structure, the F 1s peak was detected in both amorphous samples (A and B). This result corroborates the EDX semi-quantitative analysis, which demonstrated higher content of elemental F in samples A and B (6–7 at.% F) when compared with the annealed samples C and D (~ 1 at.% F). Similarly to the EDX data, carbon content (C 1s peak) was also identified in the four samples. The Ti 2p spectra (Fig. 4b) of samples A and C (non-reduced) show two peaks corresponding to Ti $2p_{3/2}$ and Ti $2p_{1/2}$ positioned at 458 eV and 464 eV, respectively, commonly attributed to the chemical state $Ti^{4+}$ in the $TiO_2$ (Wang et al., 2017). A shift of ~ 0.2 eV to higher binding-energy values is observed in the Ti 2p spectra of the reduced samples (B and D), which can be associated with changes in the oxidation state (Abdullah et al., 2020). The four spectra were deconvoluted into four peaks, where two small peaks at 456.8 and 462.8 eV were observed. These peaks are assigned to $Ti^{3+}$ species (Wang et al., 2017) and are negligible in the non-reduced samples (A and C) but represent about 1.2% of the cumulative signal in the reduced samples (B and D).

The spectra of the O 1s core level (Fig. 3c) exhibited significant differences in shape and were deconvoluted into four peaks to evaluate the contribution of each component to the cumulative signal. The predominant peak, centered at 529.9 ± 0.2 eV and denoted as $O_I$, is attributed to the bulk oxygen atom in the $TiO_2$ crystal lattice (Márquez et al., 2022). Compared with the non-reduced TNA samples, the binding

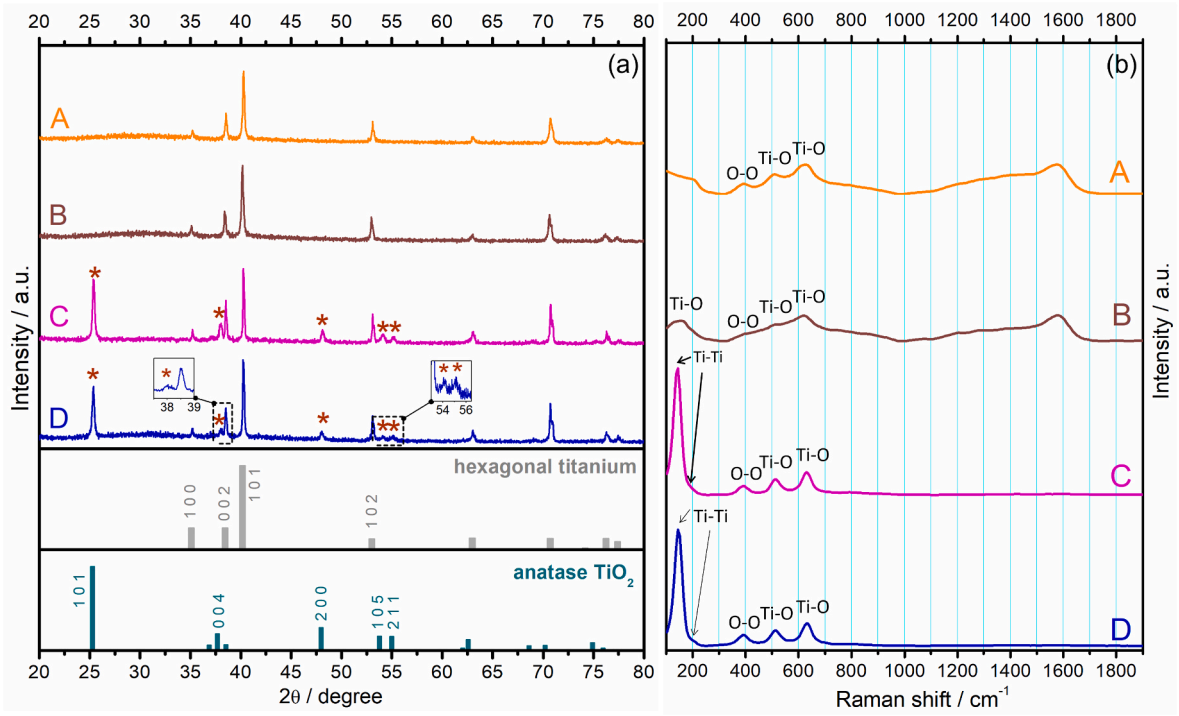


**Fig. 2.** (a) X-ray diffractograms and (b) Raman scattering spectra of TNA samples: amorphous (sample A), rd-amorphous (sample B), annealed (sample C), and rd-annealed (sample D). The standard XRD patterns of hexagonal titanium (PDF 00-044-1294) and anatase $TiO_2$ (PDF 01-086-1157) were included for comparison. The asterisk symbol indicates the anatase main peaks.

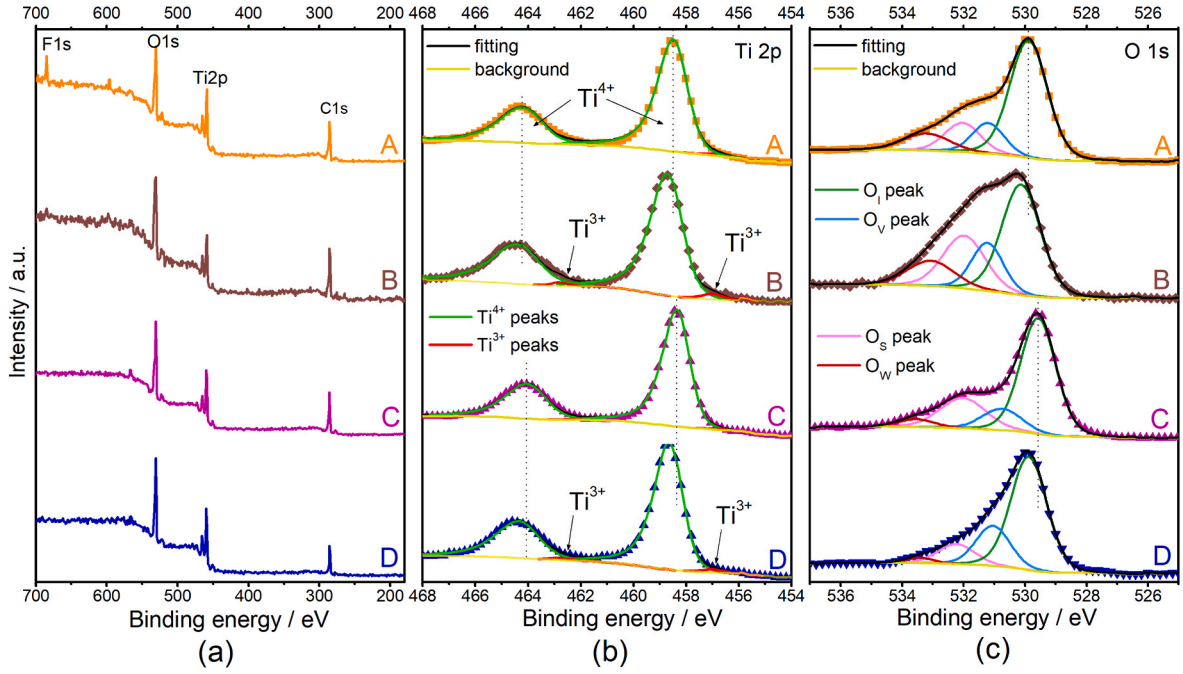


**Fig. 3.** (a) Survey XPS spectra, (b) Ti 2p spectra, and (c) O 1s spectra of samples A, B, C, and D. The symbols in (b–c) represent the experimental data, and the colored solid lines represent the fitting data and deconvoluted peaks. A = amorphous (■), B = rd-amorphous (◆), C = annealed (▲), and D = rd-annealed (▼).

energy value shifted by 0.2 eV and 0.5 eV in the rd-amorphous (B) and rd-annealed (D) samples, respectively. The peak centered at 531.1 ± 0.2 eV, denoted as $O_v$, is usually credited by researchers in the literature to chemisorbed hydroxyl groups (Flak et al., 2018) and/or to the oxygen atoms in the vicinity of an oxygen vacancy (Qin et al., 2023). Since detecting a photoelectron signal originating from a missing oxygen atom is not feasible, this latter assumption considers that introducing oxygen vacancies changes the crystal structure of the metal oxide. Comparing the $O_v$ peak area of the amorphous samples, an increase of 18% was observed going from A to B, i.e., after the cathodic reduction. In the crystalline samples, the increase after the reduction procedure was even more pronounced (40%). These results can evidence the presence of oxygen vacancies in the reduced TNA films. The peak centered at 532.1 ± 0.1 eV, denoted as $O_s$, can be attributed to oxygen ions ($O^-/O_2^{2-}$) (Flak

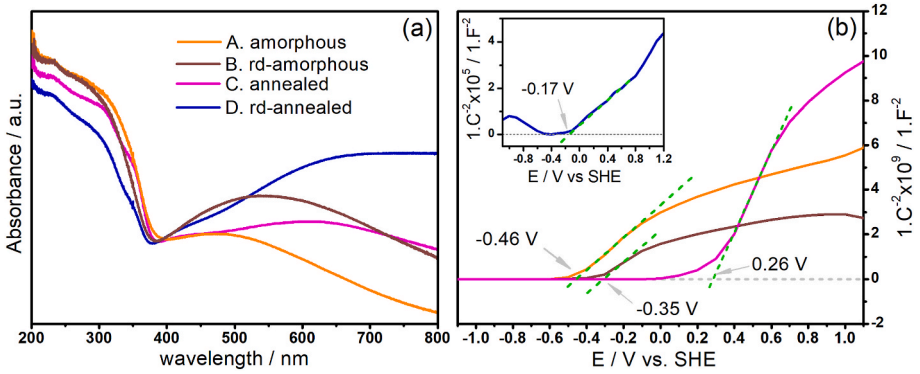


**Fig. 4.** (a) Absorption spectra and (b) Mott-Schottky plot of the TNA samples obtained in 0.1 M phosphate buffer solution (pH 7.0) saturated with $N_2$.

et al., 2018) and surface oxygen atoms located out of the amorphous/crystalline structure (Márquez et al., 2022). The small peak centered at 533.4 ± 0.2 eV, denoted as $O_w$, corresponds to physisorbed hydroxyl groups, i.e., surface-adsorbed water molecules (Márquez et al., 2022), and it is more intense in the amorphous samples (A and B).

Fig. 4a depicts the absorption spectra of the TNA films, demonstrating the main absorbance of the $TiO_2$ semiconductor in the UV range (<400 nm). However, significant differences among the samples are observed in the four spectra in the visible light range (400–700 nm). Note in this region that the non-reduced samples (A and C) presented lower absorbance when compared with the samples modified by the cathodic reduction (B and D). This result was expected since the self-doping with $Ti^{3+}$ species promoted by the cathodic reduction can enhance the semiconductor absorption under visible light irradiation (Gakhar and Hazra, 2020). Despite these differences in the visible range, the band gap ($E_g$) values found for the four samples are very similar (3.0–3.1 eV), as seen in Table 2. The band gap values were obtained from Tauc plots (Figure D1 in SI file), calculated using Tauc's equation, where $n$ was assumed as 0.5 for direct transition (Gholami et al., 2022).

### 3.2. Electrochemical and photoelectrochemical characterization

Fig. 4b depicts the Mott-Schottky plots of TNA samples measured in the dark by applying a sinusoidal perturbation of 10 mV at 1 kHz at different potentials in 0.1 M phosphate buffer solution (pH 7.0) saturated with $N_2$. The charge carrier density ($N_d$) was determined from the Mott-Schottky equation, assuming a relative permittivity of $\varepsilon = 38$ for amorphous $TiO_2$ and $\varepsilon = 50$ for anatase (Acevedo-Peña et al., 2014). Table 2 shows the flat band potential ($E_{fb}$) values for each sample, identified by extrapolation of the linear part of the MS plot. The $E_{fb}$ values found for the amorphous (A) and rd-amorphous (B) samples were −0.46 V and −0.35 V vs SHE, respectively. The difference of 0.11 V indicates a slight change in the band positions of the amorphous TNA after the cathodic reduction treatment. The $E_{fb}$ values found for the annealed and rd-annealed were 0.26 V and −0.17 V vs SHE. The change from positive to negative potential with a difference of 0.43 V indicates a significant effect of cathodic reduction on the surface properties of the annealed samples, which was also observed in the charge carrier density ($N_d$). Samples A, B, and C presented $N_d$ values in the same order of magnitude ($10^{18}$ $cm^3$) and compatible with semiconductor TNA films, as reported in the literature ($10^{17}$–$10^{19}$ $cm^3$ range) (Denisov et al., 2020; Yu et al., 2012). On the other hand, the rd-annealed sample exhibited an $N_d$ value with a magnitude 3 times higher ($10^{22}$ $cm^3$) than the other samples. This charge carrier density is within those reported for black-TNA films ($10^{21}$–$10^{23}$ $cm^3$ range), and it is ascribed to high concentrations of oxygen vacancies acting as electron donors and enhancing the conductivity of $TiO_2$ films (Zhu et al., 2018).

**Table 2**
Band gap ($E_g$) values, flat band potentials ($E_{fb}$), and the charge carrier density ($N_d$) calculated for the TNA samples.

| Sample | | $E_g$/eV | $E_{fb}$/V vs SHE | $N_d$/$cm^{-3}$ |
|---|---|---|---|---|
| A | amorphous | 3.02 | −0.46 | $2.3 \times 10^{18}$ |
| B | rd-amorphous | 3.00 | −0.35 | $3.5 \times 10^{18}$ |
| C | annealed | 3.10 | 0.26 | $0.8 \times 10^{18}$ |
| D | rd-annealed | 3.12 | −0.17 | $2.6 \times 10^{22}$ |

Fig. 5 depicts the Nyquist plots of the four samples obtained in phosphate buffer solution (pH 7.0) saturated with $N_2$ or $CO_2$. The EIS spectra of sample A (Fig. 5a) are characterized by the presence of two merged semicircles in the high-frequency domain and an increase of impedance in the low-frequency region in both experiments performed in $N_2$- and $CO_2$-saturated electrolyte. The Bode plots showing the Z modulus and the phase angle as a function of the frequency are depicted in Figure E2 – SI file. The small semicircle in the spectra of sample A spectra is not easily visible in the Nyquist plot, but the Bode plots demonstrated that the system has two-time constants. Changes in the electrolyte/semiconductor interface in the presence of $CO_2$ gas are evidenced by the modification of OCP values and impedance arc. When compared with sample A, the EIS spectra of sample B (rd-amorphous) altered significantly, exhibiting small semicircle radii and low impedance values, as can be seen in Fig. 5b and Figure E2b in the SI file. Sample B (rd-amorphous) also exhibited a slight change in impedance values in $CO_2$-saturated electrolyte in the high-frequency region (see inset in Fig. 5b). Regarding the annealed samples, the impedance arcs are not easily identified in the Nyquist plots (Fig. 5c–d) since the spectra tend to an almost vertical line, indicating mainly capacitive behavior (Atyaoui et al., 2011; Li et al., 2018b). The $N_2$- and $CO_2$-saturated spectra overlapped at moderate and high-frequency domains. The effect of $CO_2$ saturation was observed in the low-frequency domain. The impedance values in this range decreased in the $CO_2$-saturated solution compared to the $N_2$-saturated solution, as seen in the Z modulus Bode plots (Figure E2c-d).

The EC model used to describe the resistive/capacitive behavior of the TNA samples is illustrated in the SI file. The capacitor Q was replaced by a constant phase element (CPE) to include the effects of surface roughness and the adsorption of chemical species (Santos et al., 2023a). The model consists of the solution resistance ($R_s$), three resistances ($R_1$, $R_2$, and $R_3$), and three constant phase elements ($CPE_1$, $CPE_2$, and $CPE_3$), whose values are shown in Table E1 (SI file). Regarding the amorphous samples, it was observed a significant influence of $CO_2$ purging on sample B (rd-amorphous), as revealed by $R_s$ values, which comprises the effects of ionic concentration, ions type, and electrode distance, among other factors (Gholami et al., 2023). $R_s$ maintained about 11 Ω in sample A and increased from 6.4 to 16.0 Ω when the solution was saturated with $CO_2$ instead of $N_2$ (sample B). $R_1$/$CPE_1$ are associated with fast electrode/electrolyte interface processes. Some models attributed it to the processes occurring in the outer nanotube layer (Monetta et al., 2017) and resistivity inside the pores filled with solution (González et al.,

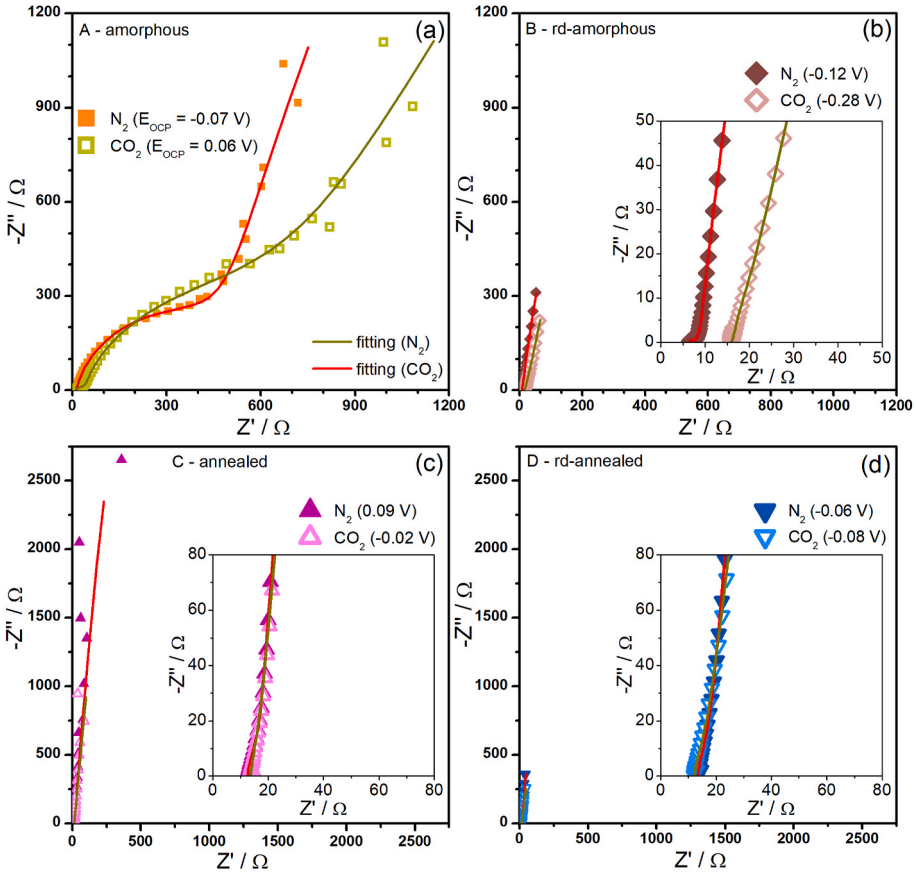


**Fig. 5.** Nyquist plots of the TNA samples obtained at OCP in phosphate buffer solution, pH 7.0, saturated with $N_2$ or $CO_2$: (a) amorphous, (b) rd-amorphous, (c) annealed, and (d) rd-annealed. The symbols represent the raw data, and the solid lines correspond to the fitting using a [R([R([R(RQ)]Q)]Q)] equivalent circuit model. The OCP values are exhibited in the SHE potential scale.

1999). $R_1$ values increased in the $CO_2$-saturated solution for both samples, but the small variation in sample B (1.6–5.5 Ω) indicates that the cathodic reduction treatment on the amorphous sample could minimize the effect of $CO_2$ saturation. The associated $CPE_1$ elements present low values ($10^{-3}$–$10^{-4}$ $\Omega^{-1}s^n$).

Regarding $R_2$, which can be attributed to the inner barrier layer resistance at the bottom of the nanotubes (Monetta et al., 2017), an increase in the values was observed in $CO_2$-saturated electrolytes in both amorphous samples (Table E1). Also, $R_2$ and $CPE_2$ values indicate less resistance of the rd-amorphous sample and improved capacitive behavior. The $R_3/CPE_3$ elements are associated with slow processes at the semiconductor surface. The high resistance values found for $R_3$ values indicate charge accumulation.

The $R_s$ values related to the annealed catalysts (12.0–13.6 Ω) were close to those of the amorphous samples. The resistance associated with the fast processes ($R_1$) also presented the same trend of the amorphous, increasing in the $CO_2$-saturated electrolyte. $R_1$ changed from 52.6 to 171 Ω in sample C (annealed) and from 66.9 to 104 Ω in sample D (rd-annealed). Regarding $R_2/CPE_2$ and $R_3/CPE_3$ elements, associated with moderate and slow processes, respectively, a more capacitive behavior was observed in the annealed samples C and D. $R_2$ and $R_3$ exhibited values in the $10^3$–$10^4$ Ω range and $n_2$ and $n_3$ ranging from 0.91 to 0.99.

The photocurrent experiments were performed by linear sweep voltammetry (LSV) and chronoamperometry (CA) in phosphate buffer solution, pH 7.0, saturated with $N_2$ or $CO_2$ in the dark and irradiated by a 1000 W Xe lamp. Before the experiments, the samples were immersed in the solution for 5400 s while OCP was monitored (Figure F1 in SI file). Another set of experiments was performed using light on/off cycles (chopped condition) to observe the instantaneous photocurrent and relaxation behavior. The LSV results are depicted in Fig. 6 and show enhanced current density under light irradiation for all conditions and a dependence on the applied potential. Except for sample C, where the current magnitude remained constant, the more positive the applied potential, the higher the current density. This increase of the (photo) current towards the positive scan can be promoted by the oxygen evolution reaction (OER). Another feature observed is that in the chopped measurements (solid line) of amorphous samples (Fig. 6a–d), photocurrent did not reach the light and dark curves (dot and dash lines, respectively) like the annealed samples (Fig. 6e–h). This behavior is closely related to the response time to the light excitation. The annealed catalysts reached the equilibrium condition faster than the amorphous ones.

Chronoamperometry (CA) measurements were performed at 1.0 V vs SHE for 300 s using a 30 s light on/off cycle to compare the current magnitude without the OER interference. The results are exhibited in Fig. 7. The CA curves show that the magnitude of the current density of the annealed samples is larger than the amorphous samples, as observed by the current increment during the light on/off cycles. Regarding the electrolyte saturation, the $CO_2$ purging decreased the current in the amorphous samples (Fig. 7a). In the annealed samples, the $CO_2$ saturation promoted an increase in the current generated by sample C but decreased the current when sample D was used (Fig. 7b).

A statistical tool was applied to the CA results to evaluate systematically and quantitatively the effects of cathodic reduction, crystallinity degree, gas purging, and light irradiation on the current generation. For this, the average current densities obtained during the on/off cycles were determined, and all conditions were combined in a $2^4$ factorial design (see Tables F1-F3 in the SI file). The methodology for calculating the variables' effects using factorial design can be found elsewhere (Santos et al., 2014). In this methodology, the effects of a variable on a

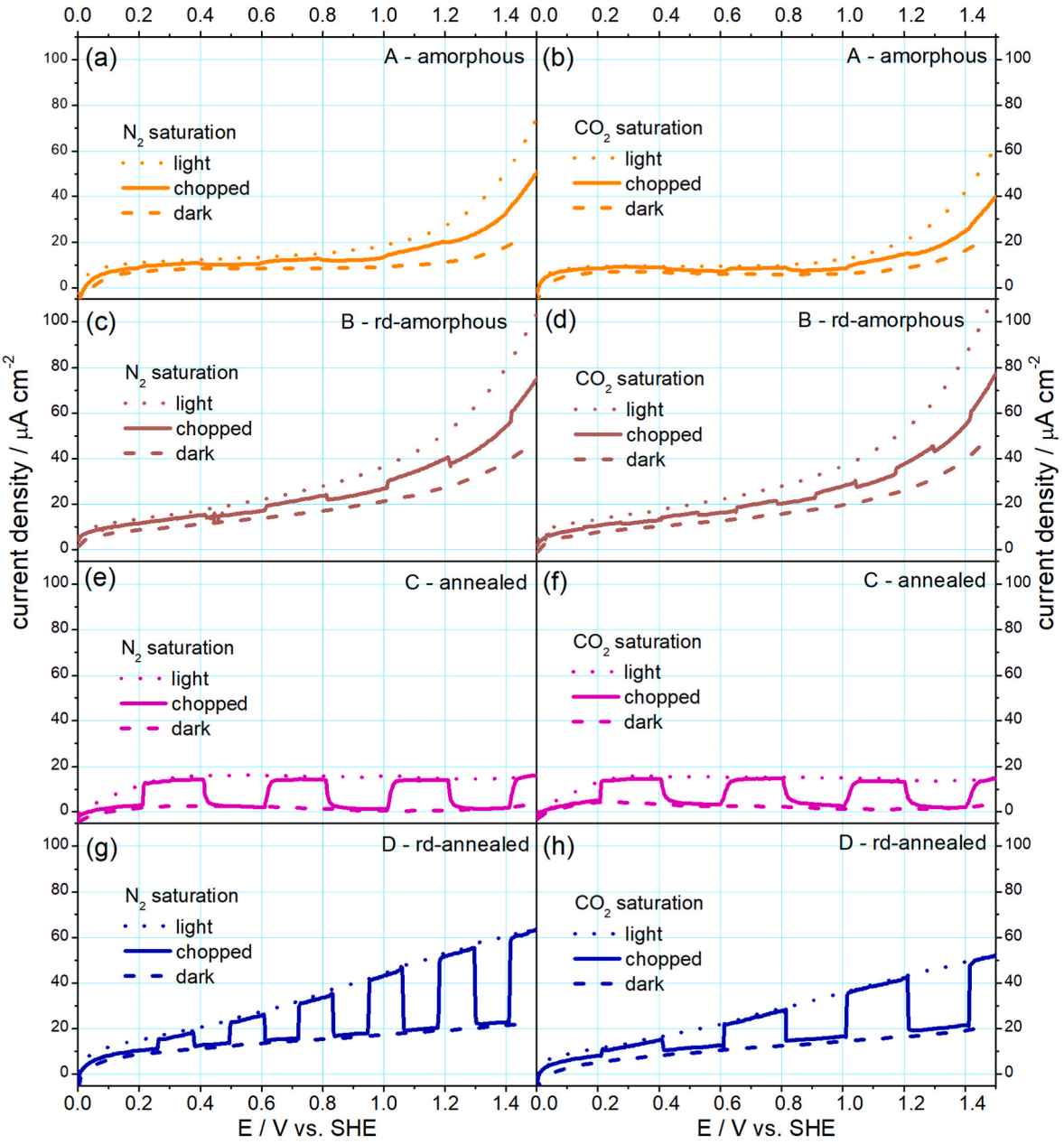


**Fig. 6.** LSV curves of TNA samples performed at 20 mV $s^{-1}$ in phosphate buffer solution, pH 7.0, saturated with $N_2$ (a, c, e, g) or $CO_2$ (b, d, f, h) under dark (dashed line), chopped (solid line), and light (dot line) conditions. Light irradiation: 1000 W Xe lamp.

specific response are determined by analysis of changes in the response when the variable is altered from the lower level to the upper level. The cross-effects (interaction effects) are also calculated. The effect of a variable on the investigated response is considered significant if its value is larger than the associated error.

Table F3 (SI file) reveals that light irradiation and cathodic reduction exhibited the highest effect on the current density among the variables. The effects of the variables followed the trend: light > cathodic reduction > crystallinity > electrolyte saturation with 9.0 ± 0.4, 6.9 ± 0.4, 2.5 ± 0.4, and −2.3 ± 0.4 μA $cm^{-2}$, respectively. The positive value indicated that the current density increased when the variable changed from lower to upper level. In this sense, the results show that the current increased by 9.0 ± 0.4 μA $cm^{-2}$ during the light irradiation. Similarly, the current increased by 6.9 ± 0.4 μA $cm^{-2}$ when the TNA film was cathodically reduced. The impact of the cathodic reduction was larger than the crystallinity since an increment of 2.5 ± 0.4 μA $cm^{-2}$ was observed after changing from amorphous to annealed samples. The negative effect of −2.3 ± 0.4 μA $cm^{-2}$ for the electrolyte saturation indicated that the current decreased 2.3 μA $cm^{-2}$ on average when the saturation was changed from $N_2$ to $CO_2$ gas.

Although the effect of crystallinity was not too high compared with other variables, the cross-effect between crystallinity and light (7.2 ± 0.4 μA $cm^{-2}$) was impressive, indicating a synergistic effect between these two variables. This result suggests that, in dark conditions, the enhanced current promoted by annealing is moderate but can be boosted significantly under light irradiation. Other significant but moderate cross-effects observed include the interaction between cathodic reduction and light (2.5 ± 0.4 μA $cm^{-2}$) and the interaction effect among cathodic reduction, crystallinity, and light (2.4 ± 0.4 μA $cm^{-2}$).

The current density values observed during the on/off cycles of the chronoamperometry experiments were used to calculate the incident photon current efficiency (IPCE), as described elsewhere (Tarek et al., 2019). The photocurrent densities of the four TNA catalysts were calculated from the difference of current densities registered during the

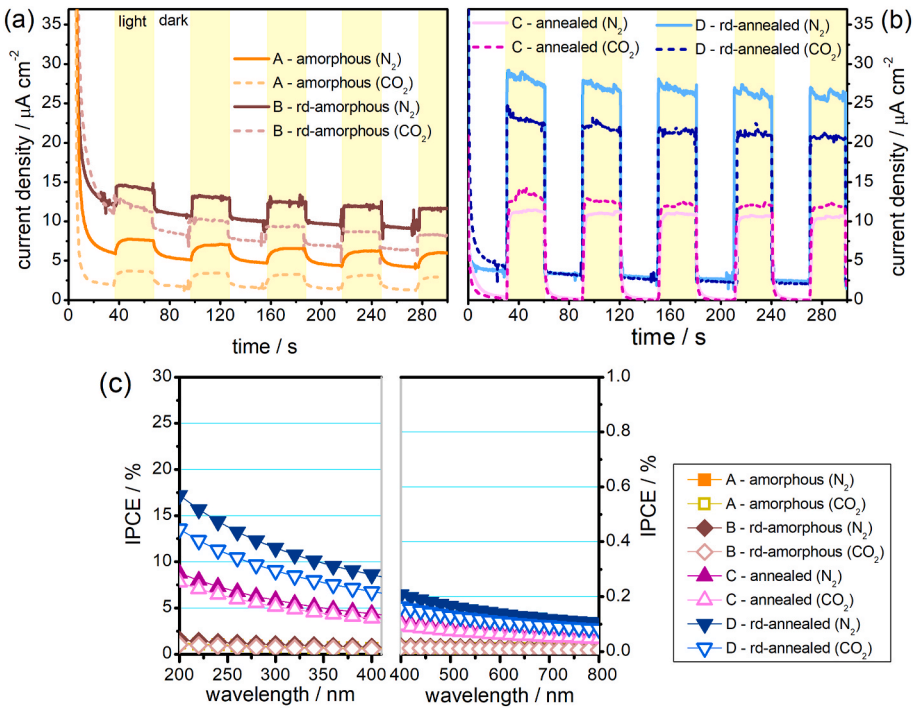


**Fig. 7.** CA curves of TNA samples in phosphate buffer solution saturated with $N_2$ or $CO_2$ in light on/off conditions: (a) amorphous and rd-amorphous catalysts and (b) annealed and rd-annealed catalysts. (c) IPCE as a function of the wavelength calculated from photocurrent generated at 1 V vs SHE in UV and visible light–infrared regions. Light irradiation: 1000 W Xe lamp.

light on and off from CA measurements. For this, the light power of the Xe lamp was measured with a radiometer using two probes: one in the UV range (8.5 mW $cm^{-2}$) and the other in the visible-infrared range (35.2 mW $cm^{-2}$), as shown in Fig. 7c. The power intensity was assumed to be constant in each wavelength range. The IPCE results revealed that sample D (rd-annealed) exhibited the highest efficiency in the UV region (200–400 nm), with values varying from 17.2 to 9.1%. Sample C (annealed) also demonstrated good efficiency, with percentages from 8.8 to 4.6% in the same spectral range. These values are in the same order of magnitude as those reported in the literature, like crystalline TNA films used in photoelectrochemical systems (Chiarello et al., 2016; Kim et al., 2022; Lee et al., 2022; Zhang et al., 2023b) and other

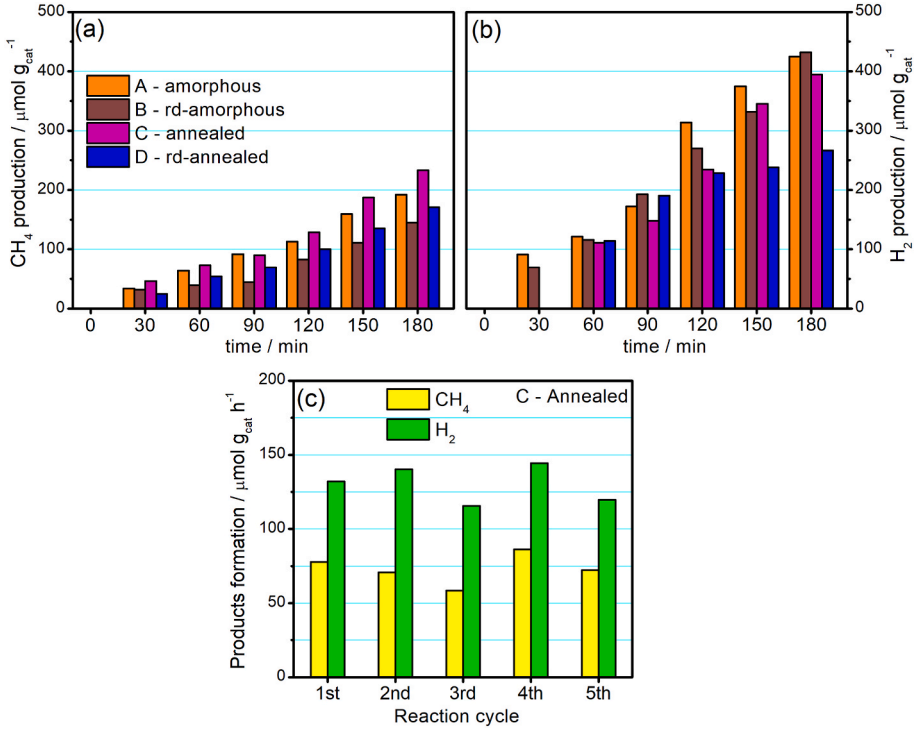


**Fig. 8.** $CO_2$ photocatalytic activity of the four synthesized catalysts in water vapor at 39 °C: (a) $CH_4$ production and (b) $H_2$ production as a function of time. (c) Stability tests performed up to five reaction cycles using the annealed catalyst (sample C).

semiconductors, like CdS–$CuFe_2O_4$ (Tarek et al., 2019) employed in $CO_2$ reduction. The electrolyte saturation with $CO_2$ decreased the IPCE values: 13.6–7.1% and 7.8–4.1% for catalysts D and C, respectively, which can be associated with a change in the processes (and possibly reactions) occurring with the $CO_2$ addition in the phosphate buffer at 1 V.

The amorphous samples presented IPCE values smaller than 2% in the UV region. Under these conditions, the IPCE in the visible and infrared spectra range can be considered negligible (<0.2%) compared with the efficiency of the samples in the UV range. Despite demonstrating good absorbance in the visible light region (Fig. 4a), catalyst D exhibited insignificant IPCE at 1 V under visible light irradiation. Similar behavior was reported for black-TNA produced by annealing under an $H_2$ atmosphere (Denisov et al., 2020). Despite significant light absorption in the visible range, the authors observed a poor photocurrent generation in this spectral range and attributed it to a short lifetime of charge carriers caused by fast recombination on the trap states below the oxygen vacancy level in the $TiO_2$ band gap.

### 3.3. Photoactivity of TNA films in $CO_2$ reduction

Fig. 8 depicts the production rate of $CH_4$ and $H_2$ detected by GC during the $CO_2$ photoreduction reaction with water vapor. Fig. 8a shows a progressive methane production for all catalysts, where the annealed catalyst (sample C) exhibited the best performance with a methane formation rate of 78 μmol $g_{cat}^{-1}$ $h^{-1}$ and a cumulative concentration of 234 μmol $g_{cat}^{-1}$ at 180 min. The amorphous catalyst (sample A) also exhibited an impressive performance, producing 192 μmol $g_{cat}^{-1}$ of $CH_4$ in 180 min at 64 μmol $g_{cat}^{-1}$ $h^{-1}$ rate. The reduced samples also showed good results but were lower than the non-reduced samples. The final $CH_4$ concentration related to samples B and D found was 145 and 171 μmol $g_{cat}^{-1}$ at 180 min with 48 and 57 μmol $g_{cat}^{-1}$ $h^{-1}$ production rates, respectively.

The methane production rates of the four synthesized catalysts and other bare TNA catalysts reported in the literature in gas phase $CO_2$ photoreduction with water vapor can be found in the SI file. Regarding the amorphous TNA (sample A), the production rate observed (64 μmol $g_{cat}^{-1}$ $h^{-1}$) is compatible with our previous result of 14 μmol $g_{cat}^{-1}$ $h^{-1}$ (Santos et al., 2022). The geometric area increased about 5 times (from 5 to 25 $cm^2$), and the production rate about 4.6 times (from 14 to 64 μmol $g_{cat}^{-1}$ $h^{-1}$), as expected. Considering the anatase film (sample C), the production rate (78 μmol $g_{cat}^{-1}$ $h^{-1}$) is within the range of those values reported for other anatase TNA films (9.5, 28.49, and 861.1 μmol $g_{cat}^{-1}$ $h^{-1}$) (Kar et al., 2019; Li et al., 2018a; Zhang et al., 2021b) and the differences can be associated with the $CO_2$ photoreduction conditions, like the TNA properties and light irradiation source.

Fig. 8b depicts the $H_2$ production measured each 30 min for 3 h during the experiments with the four photocatalysts. When compared with $CH_4$ production at 180 min, the amount of $H_2$ produced was expressive for all the samples, with a better performance of the rd-amorphous (sample B) and amorphous (sample A) photocatalysts achieving a final $H_2$ concentration of 432 and 425 μmol $g_{cat}^{-1}$ at 180 min, respectively. For the annealed samples (C and D), the $H_2$ gas was not detected in the first aliquot at 30 min, but only after 1 h, with $H_2$ amounts close to the amorphous samples. The production rates observed follow the trend: rd-amorphous (B) > amorphous (A) > annealed (C) > rd-annealed (D) with the respective formation rates: 144, 142, 132, and 89 μmol $g_{cat}^{-1}$ $h^{-1}$. These results and other values reported in the literature for $H_2$ production in $CO_2$ reduction using $TiO_2$-based photocatalysts can be found in the SI file.

Since the stability of amorphous TNA film towards $CH_4$ formation was demonstrated previously (Santos et al., 2022), the annealed film (sample C) exhibited good results for both products and was selected for stability tests. Therefore, after the first run, the catalyst was removed from the reactor, dried, and reused in a second round. This cycle was repeated five times in total. Fig. 8c shows the formation rate of $CH_4$ and $H_2$ gas products in each reaction cycle performed using the annealed catalyst. The methane production rate oscillated in the 58–78 μmol $g_{cat}^{-1}$ $h^{-1}$ range with an average of 73 ± 7 μmol $g_{cat}^{-1}$ $h^{-1}$, while the $H_2$ production rate oscillated in the 120–144 μmol $g_{cat}^{-1}$ $h^{-1}$ range with an average of 131 ± 10 μmol $g_{cat}^{-1}$ $h^{-1}$. The catalyst demonstrated high stability with no significant deactivation or decreased performance up to five reaction cycles. This result is similar to those reported in gas phase $CO_2$ conversion to $CH_4$ by Kar and co-authors using flame-annealed TNA films as photocatalysts (Kar et al., 2019) and those reported for amorphous TNA photocatalyst (Santos et al., 2022).

Fig. 9 shows the diagram with band positions used to find the possible reaction pathways for $CO_2$ conversion to $CH_4$ and $H_2$ at the TNA film surface. The position of the conduction band (CB) was determined from the flat band positions, and the position of the valence bands (VB) was calculated from the bandgap (Table 2). Since the position of the VB edge is more positive than the potential of $CO_2$ reduction to $CH_4$ and the position of the CB edge is more negative than the potential required for water oxidation to $H^+$, both $CO_2$ reduction to $CH_4$ and water oxidation reactions are thermodynamically favored (Fereidooni et al., 2023a). On the other hand, for efficient $H_2$ production, the CB level of the semiconductor should be more negative than the water reduction level ($H^+/H_2$), while the VB level should be more positive than the water oxidation level to produce $O_2$ to supply the required electrons for the water reduction to hydrogen (Gholami et al., 2021; Ismael, 2021). These criteria were achieved by the TNA electrodes, except for sample C, in which CB is more positive than the water discharge reactions. However, the results indicated that this sample was very active for $CH_4$ and $H_2$ products.

This apparent contradictory result related to the CB position of the annealed catalyst can be explained by the nature of the Mott-Schottky analysis. Similar behavior was discussed in some publications and correlated with the porous nature of the TNA films (Díaz-Real et al., 2018; Muñoz, 2007). According to some models, the $E_{fb}$ is sensitive to the nanostructure of the films and oxide layer thickness. The distribution of bandgap states is not uniform along the length and wall thickness, leading to deviation of the MS curves. According to Muñoz (2007), only the bottom of the porous film responds to the perturbation and the major contribution to the surface effects is in the pore walls. In this sense, the MS results can be used as a first approach, but it can be assumed that spectra might not represent the whole information of the nanostructured system but only the barrier film layer, i.e., the nanotubes bottom. Another factor to consider is the morphological features of the annealed catalyst, which exhibited the shortest thickness and absence of nanograss at the top, which could have affected its photocatalytic activity. The short thickness (2.2 μm), when compared with the others (3.1–3.3 μm), could offer a short pathway for charge transfers from the surface until the current collector, the metallic titanium; on the other hand, the absence of residual material on the top could dimmish the recombination rate of the electrons and holes favoring the formation of the products.

The methane production is usually explained by an enrichment of the surface electron density induced by the catalyst, which favors the multielectron process required for $CH_4$ formation (Shehzad et al., 2018). On the other hand, when the electron density is lower, CO is the preferable product. Despite $H_2$ gas not being commonly reported among the products in this type of system (bare $TiO_2$ photocatalyst + water vapor), the possibility of water splitting producing $H_2$ should be considered since the water molecules are the source of protons. The $CO_2$ photoreduction experiments using the four synthesized catalysts were performed in the water vapor at 39 °C under UV light irradiation, while the products formation was monitored by GC each 30 min for 3 h. $CH_4$ and $H_2$ were identified as products. Since CO was not detected among the products, the general chemical reactions involved in the process can be described by Eqs. (3)–(6).

$$TiO_2 \xrightarrow{h\nu} h^+ + e^- \quad (3)$$

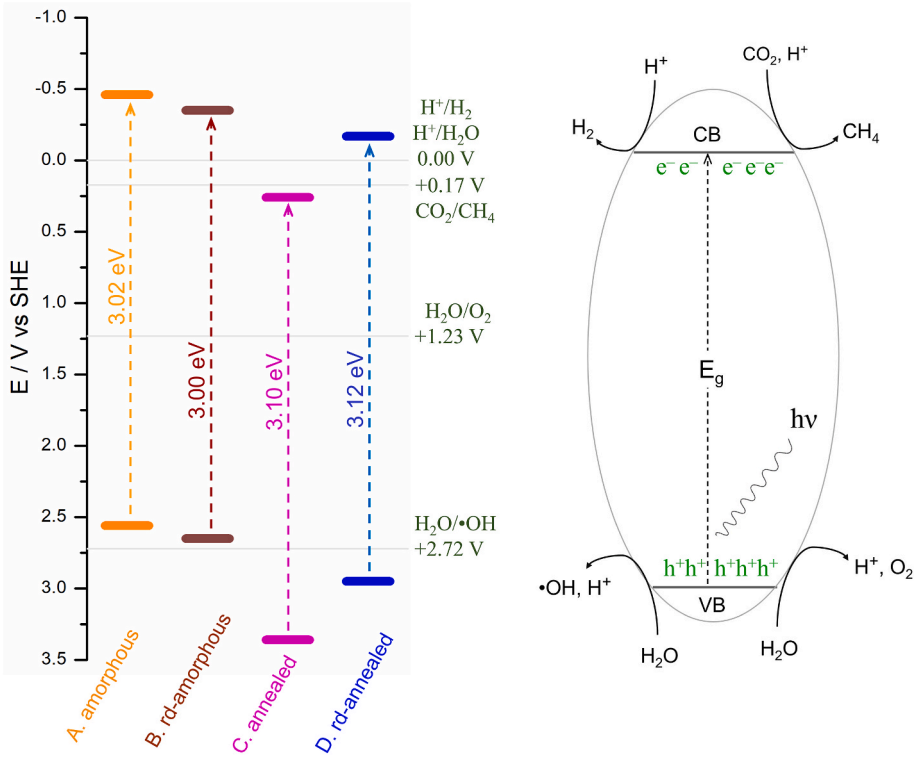


**Fig. 9.** Band positions of the four TNA catalysts and schematic illustration showing the possible chemical reactions occurring during the $CO_2$ photoreduction.

$$2H_2O + 4h^+ \overset{TiO_2}{\rightarrow} 4H^+ + O_2 \quad (4)$$

$$2H^+ + 2e^- \rightarrow H_2 \quad (5)$$

$$CO_2 + 8H^+ + 8e^- \rightarrow CH_4 + 2H_2O \quad (6)$$

The photoluminescence (PL) analysis was used to elucidate the distinctive emission peaks of various defect states in the catalyst, providing insights into the presence and distribution of defects that affect the catalyst properties (SI file). The emission peaks observed in the PL spectra of all catalysts at 396 nm (corresponding to a photon energy of 3.1 eV) can be attributed to the radiative recombination of charge carriers from the CB. All the catalysts exhibit similar emissions at wavelengths above 400 nm. The emissions within the 400–550 nm range are commonly associated with surface defects, such as $O_v$ and $Ti^{3+}$, which give rise to the formation of energy states below the CB. These defect-induced energy states act as electron traps. In addition, the emission peak at around 560 nm could be attributed to the interstitial $Ti^{3+}$ defects (Mazierski et al., 2016; Nishanthi et al., 2015). Moreover, the intense red emission peak at 610 nm has been linked to oxygen interstitials and the color center of the $TiO_2$ (Machreki et al., 2023).

Furthermore, a broad emission peak below 369 nm is observed for sample C (annealed) obtained at 280 nm excitation for better visualization (SI file). This wide emission peak, in which energy exceeded the catalyst bandgap, could stem from the recombination of charge carriers from states above the conduction band minimum (CBM) or be attributed to the anatase $TiO_2$ structure in the barrier film. Despite the lower intensity, this broad emission peak was also observed in the PL spectra of other samples. Upon the formation of $O_v$ in the catalysts, a slight decrease in emission intensity was observed, likely due to charge carrier trapping by defects or an increase in non-radiative recombination caused by the formation of defect-induced intra-band energy states (Choudhury and Choudhury, 2014; Zhang et al., 2023a).

### 3.4. Theoretical studies

A density of states (DOS) simulation was performed to understand how surface defects affect the band structure of the amorphous and crystalline $TiO_2$ films. For a defect-free amorphous $TiO_2$ (Fig. 10a), a bandgap of 2.73 eV was achieved (Fig. 10b). Upon creation of one oxygen vacancy ($O_v$) (Fig. 10c), additional electronic states appeared below the CBM, mainly originating from Ti 3d orbitals (Fig. 10d). The formation of these energy states resulted in a bandgap narrowing to 1.53 eV. After removing the second oxygen, generating two oxygen vacancies (Fig. 10e), electronic states appeared above the VB maximum (VBM), further narrowing the bandgap to 0.80 eV (Fig. 10f). Although these calculated bandgaps are not representative of the empirical bandgaps in the synthesized catalysts, the simulation of the band structure allows exploring the formation of electronic states upon $O_V$ creation (defects), which can play a significant role in trapping charge carriers and affecting catalyst activity. Therefore, introducing $O_v$ can result in the formation of electronic states below CBM and above the VBM, tailoring not only the bandgap but also the band structure.

The band structure of the crystalline anatase $TiO_2$ (101) was also simulated (Fig. 11a). The calculated bandgap of the Ov-free anatase was 3.20 eV (Fig. 11b), which was closer to the measured values (3.10–3.12 eV, see Table 2). This model is consistent with other DOS plots for bulk anatase $TiO_2$ reported in the literature, where the valence band maximum (VBM) is predominantly O 2p states, and the CBM is mostly Ti d states (Hossain et al., 2010; Quesada-Gonzalez et al., 2018; Wang et al., 2009). The formation of one $O_v$ (Fig. 11c) led to a bandgap narrowing to 2.99 eV by altering the CBM (Fig. 11d).

Regarding the atomic models in Figs. 10 and 11, the formation of one $O_v$ in the amorphous structure did not lead to creation of a localized $O_v$ site and coexistence of $O_v$ and $Ti^{3+}$ (observable in the anatase $TiO_2$ (Fig. 11c)). In the amorphous structure, the atomic rearrangement resulted in variations in the atomic coordination environment, and $O_v$ and $Ti^{3+}$ did not co-exist. Therefore, the mechanism of $CO_2$ reduction on amorphous $TiO_2$ with oxygen vacancies is likely different from that on

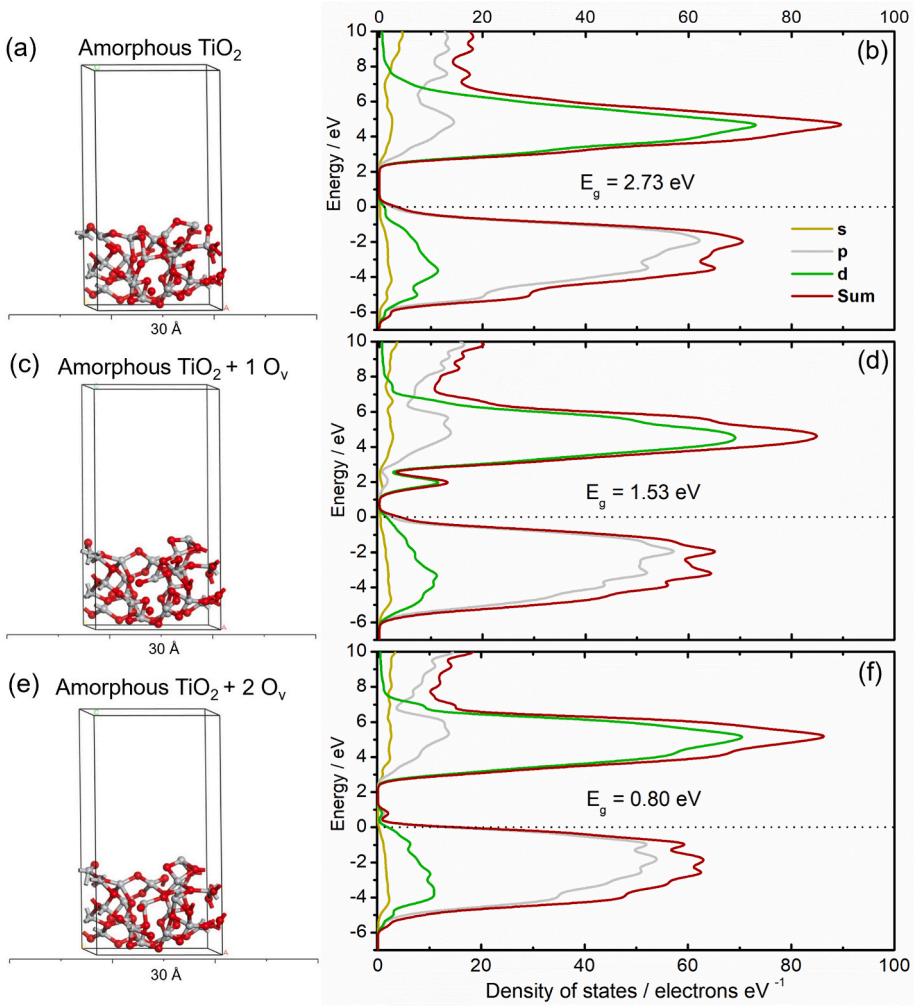


**Fig. 10.** Simulation boxes and DOS plots for an amorphous $TiO_2$ model (a–b) with no oxygen vacancy ($O_v$), (c–d) with one $O_v$, and (e–f) with two $O_v$. The oxygen atoms in the model are represented by red, and titanium atoms are represented by grey. The dotted line in the DOS plot represents the Fermi level.

crystalline $TiO_2$ with oxygen vacancies. Further research is required to elucidate the exact mechanism.

### 3.5. *Performance of TNA films*

The four TNA catalysts demonstrated remarkable photoactivity for $CO_2$ conversion to methane with simultaneous formation of $H_2$ gas from water splitting with different yields. These results indicated that amorphous and crystalline films can have different reaction mechanisms due to differences in their properties, especially their band structure. Regarding the post-treatments, the heat treatment led to more significant differences in their intrinsic properties than the cathodic reduction post-treatment, which mainly affected the oxide surface. The annealed film, consisting essentially of the anatase phase, exhibited better performance towards methane formation and high stability without significant deactivation in five reaction cycles. The annealed sample also demonstrated good stability of the photocurrent generated in a wide potential range and in impedance analysis, not altering its properties in $CO_2$-saturated electrolyte. The morphology might also influence the results since the annealed catalyst exhibited a clean nanotubular morphology, i.e., without residual oxide and with the shortest thickness layer among the four catalysts.

On the other hand, the amorphous TNA also demonstrated impressive results for $CH_4$ formation. For the $H_2$ production, the amorphous and rd-amorphous samples presented a slightly better performance than the annealed catalyst (sample C). The EIS data demonstrated that both amorphous films were more sensitive to purging, indicating a change in the capacitive behavior and interfacial processes in $CO_2$-saturated electrolyte. This change could be attributed to OH groups in the structure and residual oxide on the TNA top in the form of nanograss and nanofilm interacting with $CO_2$ dissolved into the electrolyte.

Regarding the introduction of defective $Ti^{3+}$ and oxygen vacancies into the oxide film, the results provided insights into how these defects can change the band structure of TNA film. These species are usually credited for enhancing the photoactivity of $TiO_2$. However, the reduced samples did not increase the photocatalytic efficiency. One hypothesis for this is that the cathodic reduction procedure might have enhanced the photoactivity of the catalyst but not decreased the electron-pair recombination rate, maintaining a net overall performance similar to the non-reduced photocatalysts. Another hypothesis is related to the light irradiation source since these defects aim to narrow the bandgap to sensitize the titania absorption under sunlight. This latter assumption is supported by the statistical analysis of the photocurrent results, which were performed using a wide-range spectral lamp. These results demonstrated that the "cathodic reduction" variable exerted a significant effect on the "current density" response, improving it by 6.9 μA $cm^{-2}$.

The difference in the final concentration of $H_2$ between annealed and rd-annealed samples (132 and 89 μmol $g_{cat}^{-1}$ $h^{-1}$) suggested a possible route for tuning the properties of the anatase TNA to improve its selectivity towards methane. Similarly, to improve selectivity towards $H_2$ production, a possible route is tailoring the properties of rd-

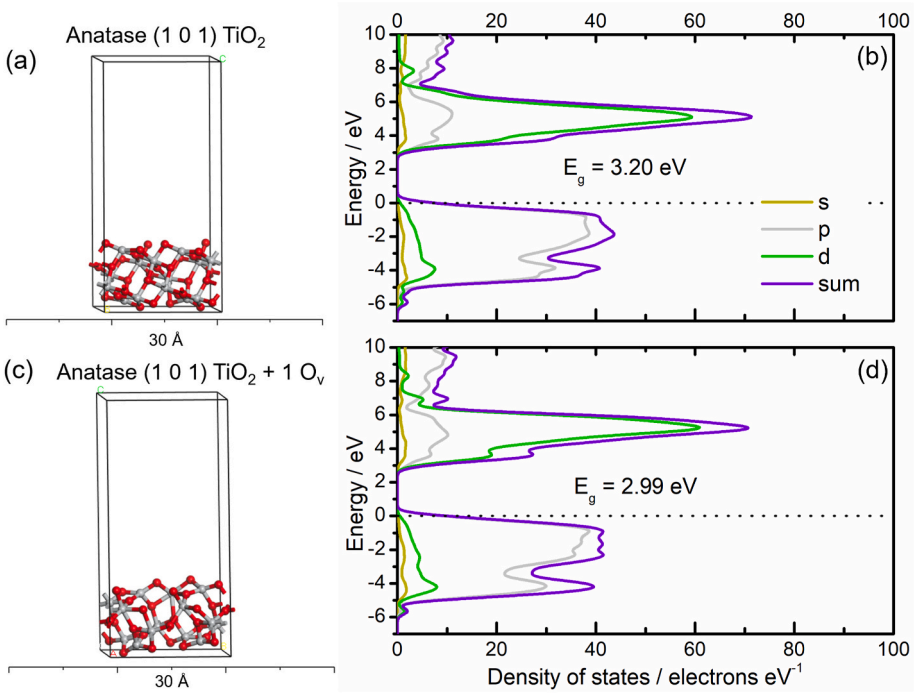


**Fig. 11.** Simulation boxes and DOS plots for anatase (101) plane (a–b) with no oxygen vacancies ($O_v$) and (c–d) with one $O_v$. The oxygen atoms in the model are represented by red and titanium atoms are represented by grey. The dotted line in DOS plot represents the Fermi level.

amorphous film for photocatalytic water splitting.

## 4. Conclusions

This study assessed the photocatalytic activity of amorphous and crystalline TNA films in gas-phase $CO_2$ photoreduction with water under UV irradiation, where $CH_4$ and $H_2$ were identified as products. The influence of interfacial defects, like $Ti^{3+}$ and oxygen vacancies, on TNA properties were also evaluated. The cathodic reduction treatment had a significant effect on the generated photocurrent. However, the reduced samples did not enhance the $CO_2$ photoreduction conversion. The following trend was observed for the four catalysts in methane production rate: annealed > amorphous > rd-annealed > rd-amorphous (78, 64,57, and 48 μmol $g_{cat}^{-1}$ $h^{-1}$, respectively). The catalysts also exhibited significant photoactivity regarding $H_2$ formation, following the trend: rd-amorphous > amorphous > annealed > rd-annealed (142, 144, 132 and 89 μmol $g_{cat}^{-1}$ $h^{-1}$, respectively). The results also demonstrated high stability of the annealed sample up to five reaction cycles. The correlation among the semiconductor properties, photocatalytic performance and simulation studies indicated that amorphous and annealed catalysts have different mechanisms for $CO_2$ reduction and provided information to guide their modification to improve the selectivity towards methane. These findings can contribute to the design of TNA-based photocatalysts with enhanced efficiency, selectivity, and durability. Additionally, the simple synthetic route, high stability, and dual functionality of the TNA films ($CO_2$ reduction and $H_2$ production) make the material promising for renewable fuel production.

## CRediT authorship contribution statement

**Janaina S. Santos:** Conceptualization, Methodology, Investigation, Formal analysis, Writing – original draft. **Mohammad Fereidooni:** Conceptualization, Investigation, Formal analysis, Writing – review & editing. **Victor Márquez:** Investigation, Writing – review & editing. **Christian V. Paz-López:** Investigation, Writing – review & editing. **Martin S. Villanueva:** Writing – review & editing, Resources. **Josephus G. Buijnsters:** Writing – review & editing, Supervision. **Supareak Praserthdam:** Writing – review & editing, Supervision. **Piyasan Praserthdam:** Writing – review & editing, Supervision, Resources.

## Declaration of competing interest

The authors declare that they have no known competing financial interests or personal relationships that could have appeared to influence the work reported in this paper.

## Data availability

Data will be made available on request.

## Acknowledgments

This research project is supported by the Second Century Fund (C2F), Chulalongkorn University, Thailand. The authors also thank the NSRF (Thailand) via the Program Management Unit for Human Resources & Institutional Development, Research, and Innovation [grant number B13F6654].

## Appendix A. Supplementary data

Supplementary data to this article can be found online at https://doi.org/10.1016/j.envres.2023.117919.

## References

Abdullah, S.A., et al., 2020. Neutron beam interaction with rutile $TiO_2$ single crystal (1 1 1): Raman and XPS study on $Ti^{3+}$-oxygen vacancy formation. Mater. Lett. 263, 127143 https://doi.org/10.1016/j.matlet.2019.127143.

Acevedo-Peña, P., et al., 2014. Effect of heat treatment on the crystal phase composition, semiconducting properties and photoelectrocatalytic color removal efficiency of $TiO_2$ nanotubes arrays. Electrochim. Acta 140, 564–571. https://doi.org/10.1016/j.electacta.2014.06.056.

Ali, G., et al., 2011. Fabrication of complete titania nanoporous structures via electrochemical anodization of Ti. Nanoscale Res. Lett. 6, 332. https://doi.org/10.1186/1556-276X-6-332.

Atyaoui, A., et al., 2011. Influence of geometric and electronic characteristics of $TiO_2$ electrodes with nanotubular array on their photocatalytic efficiencies. J. Photochem. Photobiol., A 224, 71–79. https://doi.org/10.1016/j.jphotochem.2011.09.009.

Babaie-Aghdam, S., et al., 2023. Morphological evolution of sol-electrophoretic deposited ZnO nanostructures on anodic TiO2 nanotubes for back-side illuminated dye-sensitised solar cells. Mater. Res. Bull. 160, 112134 https://doi.org/10.1016/j.materresbull.2022.112134.

Bharti, B., et al., 2016. Formation of oxygen vacancies and $Ti^{3+}$ state in $TiO_2$ thin film and enhanced optical properties by air plasma treatment. Sci. Rep. 6, 32355 https://doi.org/10.1038/srep32355.

Cheng, M., et al., 2021. Highly efficient photocatalytic conversion of gas phase $CO_2$ by $TiO_2$ nanotube array sensitized with CdS/ZnS quantum dots under visible light. Int. J. Hydrogen Energy 46, 31634–31646. https://doi.org/10.1016/j.ijhydene.2021.07.067.

Cheng, Y., et al., 2022. In situ electrochemical reduced Au loaded black $TiO_2$ nanotubes for visible light photocatalysis. J. Alloys Compd. 901, 163562 https://doi.org/10.1016/j.jallcom.2021.163562.

Chiarello, G.L., et al., 2016. Exploiting the photonic crystal properties of $TiO_2$ nanotube arrays to enhance photocatalytic hydrogen production. ACS Catal. 6, 1345–1353. https://doi.org/10.1021/acscatal.5b02817.

Choudhury, B., Choudhury, A., 2014. Oxygen defect dependent variation of band gap, Urbach energy and luminescence property of anatase, anatase–rutile mixed phase and of rutile phases of $TiO_2$ nanoparticles. Physica E: Low Dimens. Syst. Nanostruct. 56, 364–371. https://doi.org/10.1016/j.physe.2013.10.014.

Denisov, N., et al., 2020. Photoelectrochemical properties of "increasingly dark" $TiO_2$ nanotube arrays. J. Electroanal. Chem. 872, 114098 https://doi.org/10.1016/j.jelechem.2020.114098.

Díaz-Real, J.A., et al., 2018. Impact of the anodization time on the photocatalytic activity of $TiO_2$ nanotubes. Beilstein J. Nanotechnol. 9, 2628–2643. https://doi.org/10.3762/bjnano.9.244.

Domínguez-Espíndola, R.B., et al., 2022. A critical review on advances in $TiO_2$-based photocatalytic systems for $CO_2$ reduction. Appl. Therm. Eng., 119009 https://doi.org/10.1016/j.applthermaleng.2022.119009.

Fan, W.K., Tahir, M., 2022. Recent developments in photothermal reactors with understanding on the role of light/heat for $CO_2$ hydrogenation to fuels: a review. Chem. Eng. J. 427, 131617 https://doi.org/10.1016/j.cej.2021.131617.

Fereidooni, M., et al., 2023a. On the $CO_2$ photocatalytic reduction over indium tin oxide (ITO) ultra-thin films in water vapor: experimental and theoretical study. Fuel 349, 128652. https://doi.org/10.1016/j.fuel.2023.128652.

Fereidooni, M., et al., 2023b. Effect of substrate conductivity on charge transfer and CO2 photoreduction in water vapor over silica-modified TiO2 films. Appl. Surf. Sci. 611, 155595 https://doi.org/10.1016/j.apsusc.2022.155595.

Flak, D., et al., 2018. In situ ambient pressure XPS observation of surface chemistry and electronic structure of $\alpha$-$Fe_2O_3$ and $\gamma$-$Fe_2O_3$ nanoparticles. Appl. Surf. Sci. 455, 1019–1028. https://doi.org/10.1016/j.apsusc.2018.06.002.

Fu, Z., et al., 2019. Photocatalytic conversion of carbon dioxide: from products to design the catalysts. J. CO2 Util. 34, 63–73. https://doi.org/10.1016/j.jcou.2019.05.032.

Gakhar, T., Hazra, A., 2020. Oxygen vacancy modulation of titania nanotubes by cathodic polarization and chemical reduction routes for efficient detection of volatile organic compounds. Nanoscale 12, 9082–9093. https://doi.org/10.1039/C9NR10795A.

Gao, J., et al., 2020. Oxygen vacancy self-doped black $TiO_2$ nanotube arrays by aluminothermic reduction for photocatalytic $CO_2$ reduction under visible light illumination. J. CO2 Util. 35, 205–215. https://doi.org/10.1016/j.jcou.2019.09.016.

Gholami, P., et al., 2023. Oxygen and nitrogen plasma modifications of ZnCuCo LDH-graphene nanocomposites for photocatalytic hydrogen production and antibiotic degradation. Sep. Purif. Technol. 325, 124706 https://doi.org/10.1016/j.seppur.2023.124706.

Gholami, P., et al., 2020. Photocatalytic degradation of antibiotic and hydrogen production using diatom-templated 3D WO3-x@mesoporous carbon nanohybrid under visible light irradiation. J. Clean. Prod. 275, 124157 https://doi.org/10.1016/j.jclepro.2020.124157.

Gholami, P., et al., 2021. Synthesis of N-doped Magnetic WO3–x@Mesoporous carbon using a diatom Template and plasma modification: visible-light-driven photocatalytic Activities. ACS Appl. Mater. Interfaces 13, 13072–13086. https://doi.org/10.1021/acsami.0c21076.

Gholami, P., et al., 2022. Template-free hierarchical trimetallic oxide photocatalyst derived from organically modified ZnCuCo layered double hydroxide. J. Clean. Prod. 366, 132761 https://doi.org/10.1016/j.jclepro.2022.132761.

Giziński, D., et al., 2020. Nanostructured anodic copper oxides as catalysts in electrochemical and photoelectrochemical reactions. Catalysts 10, 1338. https://doi.org/10.3390/catal10111338.

González, J.A., et al., 1999. Characterization of porous aluminium oxide films from a.c. impedance measurements. J. Appl. Electrochem. 29, 229–238. https://doi.org/10.1023/A:1003481418291.

Goto, H., et al., 2022. Intricate behaviors of gas phase CO2 photoreduction in high vacuum using Cu2O-loaded TiO2 nanotube arrays. J. CO2 Util. 59, 101964 https://doi.org/10.1016/j.jcou.2022.101964.

Hardcastle, F.D., et al., 2011. Photoelectroactivity and Raman spectroscopy of anodized titania ($TiO_2$) photoactive water-splitting catalysts as a function of oxygen-annealing temperature. J. Mater. Chem. 21, 6337–6345. https://doi.org/10.1039/C0JM03106B.

Hossain, F.M., et al., 2010. Electronic and optical properties of anatase $TiO_2$ nanotubes. Comput. Mater. Sci. 48, 854–858. https://doi.org/10.1016/j.commatsci.2010.04.007.

Hossen, M.A., et al., 2022. A comprehensive review on advances in $TiO_2$ nanotube (TNT)-Based photocatalytic $CO_2$ reduction to value-added products. Energies 15.

Ismael, M., 2021. Latest progress on the key operating parameters affecting the photocatalytic activity of $TiO_2$-based photocatalysts for hydrogen fuel production: a comprehensive review. Fuel 303, 121207. https://doi.org/10.1016/j.fuel.2021.121207.

Jardak, K., et al., 2017. Statistical optimization of electrochemical oxidation of ethylene glycol using response surface methodology. PSEP 105, 12–20. https://doi.org/10.1016/j.psep.2016.08.021.

Kar, P., et al., 2019. High rate $CO_2$ photoreduction using flame annealed $TiO_2$ nanotubes. Appl. Catal., B 243, 522–536. https://doi.org/10.1016/j.apcatb.2018.08.002.

Kharade, A.K., Chang, S.-m., 2020. Contributions of Abundant hydroxyl groups to Extraordinarily high photocatalytic activity of amorphous titania for $CO_2$ reduction. J. Phys. Chem. C 124, 10981–10992. https://doi.org/10.1021/acs.jpcc.0c01548.

Khatun, F., et al., 2019. Plasmonic enhanced Au decorated $TiO_2$ nanotube arrays as a visible light active catalyst towards photocatalytic $CO_2$ conversion to $CH_4$. J. Environ. Chem. Eng. 7, 103233 https://doi.org/10.1016/j.jece.2019.103233.

Kim, D., et al., 2008. $TiO_2$ Nanotube arrays: Elimination of disordered top layers ("nanograss") for improved photoconversion efficiency in dye-sensitized solar cells. Electrochem. Commun. 10, 1835–1838. https://doi.org/10.1016/j.elecom.2008.09.029.

Kim, T., et al., 2022. Nanospace-confined worm-like $BiVO_4$ in $TiO_2$ space nanotubes (SPNTs) for photoelectrochemical hydrogen production. Electrochim. Acta 432, 141213. https://doi.org/10.1016/j.electacta.2022.141213.

Lamberti, A., et al., 2015. Ultrafast room-temperature crystallization of $TiO_2$ nanotubes Exploiting water-vapor treatment. Sci. Rep. 5, 7808. https://doi.org/10.1038/srep07808.

Lee, J., et al., 2022. Visible photoresponse of $TiO_2$ nanotubes in comparison to that of nanoparticles and anodic thin film. Catal. Today 403, 39–46. https://doi.org/10.1016/j.cattod.2022.01.008.

Li, D., et al., 2018a. Enhanced activity of $TiO_2$ by concentrating light for photoreduction of $CO_2$ with $H_2O$ to $CH_4$. Catal. Commun. 113, 6–9. https://doi.org/10.1016/j.catcom.2018.05.005.

Li, Y., et al., 2018b. Structural, morphological and electrochemical properties of long alkoxy-functionalized polythiophene and $TiO_2$ nanocomposites. Appl. Phys. A 124, 855. https://doi.org/10.1007/s00339-018-2277-y.

Machreki, M., et al., 2023. The role of lattice defects on the optical properties of $TiO_2$ nanotube arrays for synergistic water splitting. ACS Omega. https://doi.org/10.1021/acsomega.3c00965.

Márquez, V., et al., 2022. Effect of the annealing temperature of multi-elemental oxides $(FeCoNiCuZn)_yO_x$ on the electrocatalytic hydrogenation of nitrobenzene at room temperature. Electrochim. Acta 428, 140975. https://doi.org/10.1016/j.electacta.2022.140975.

Mazierski, P., et al., 2016. Photocatalytic activity of nitrogen doped $TiO_2$ nanotubes prepared by anodic oxidation: the effect of applied voltage, anodization time and amount of nitrogen dopant. Appl. Catal., B 196, 77–88. https://doi.org/10.1016/j.apcatb.2016.05.006.

Monetta, T., et al., 2017. $TiO_2$ nanotubes on Ti Dental implant. Part 2: EIS characterization in Hank's solution. Metals 7. https://doi.org/10.3390/met7060220.

Muñoz, A.G., 2007. Semiconducting properties of self-organized $TiO_2$ nanotubes. Electrochim. Acta 52, 4167–4176. https://doi.org/10.1016/j.electacta.2006.11.035.

Nishanthi, S.T., et al., 2015. An insight into the influence of morphology on the photoelectrochemical activity of $TiO_2$ nanotube arrays. Sol. Energy Mater. Sol. Cells 132, 204–209. https://doi.org/10.1016/j.solmat.2014.09.005.

Pardanaud, C., et al., 2019. Investigating the Possible Origin of Raman Bands in Defective $Sp^2/sp^3$ Carbons below 900 $Cm^{-1}$: Phonon Density of States or Double Resonance Mechanism at Play?, vol. 5. C. https://doi.org/10.3390/c5040079.

Paz-López, C.V., et al., 2023. Comprehensive analysis (aerobic/anaerobic, molecular recognitions, band-position and degradation-mechanism) of undoped and Co-doped anatase-brookite - an experimental/theoretical evaluation of the less-studied $TiO_2$ mixed phase. Environ. Res. 229, 115968 https://doi.org/10.1016/j.envres.2023.115968.

Paz, C.V., et al., 2022. Toward the understanding of surface phenomena involved in the photocatalytic performance of amorphous $TiO_2/SiO_2$ catalyst – a theoretical and experimental study. Appl. Surf. Sci. 588, 152920 https://doi.org/10.1016/j.apsusc.2022.152920.

Qian, X., et al., 2020. Highly selective, defect-induced photocatalytic $CO_2$ reduction to Acetaldehyde by the Nb-doped $TiO_2$ nanotube array under simulated solar illumination. ACS Appl. Mater. Interfaces 12, 55982–55993. https://doi.org/10.1021/acsami.0c17174.

Qin, H., et al., 2023. Synergistic Engineering of doping and vacancy in $Ni(OH)_2$ to Boost Urea Electrooxidation. Adv. Funct. Mater. 33, 2209698 https://doi.org/10.1002/adfm.202209698.

Quesada-Gonzalez, M., et al., 2018. Deeper understanding of interstitial boron-doped anatase thin films as A Multifunctional layer through theory and experiment. J. Phys. Chem. C 122, 714–726. https://doi.org/10.1021/acs.jpcc.7b11142.

Rambabu, Y., et al., 2019. Photocatalytic reduction of carbon dioxide using graphene oxide wrapped $TiO_2$ nanotubes. Appl. Surf. Sci. 485, 48–55. https://doi.org/10.1016/j.apsusc.2019.04.041.

Sánchez, E., et al., 1996. Synthesis and characterization of sol–Gel $Pt/TiO_2$ catalyst. J. Solid State Chem. 122, 309–314. https://doi.org/10.1006/jssc.1996.0118.

Santos, J.S., et al., 2021. The Use of anodic oxides in Practical and sustainable Devices for energy conversion and storage. Materials 14, 383. https://doi.org/10.3390/ma14020383.

Santos, J.S., et al., 2022. Single-step fabrication of highly stable amorphous $TiO_2$ nanotubes arrays (am-TNTA) for stimulating gas-phase photoreduction of $CO_2$ to methane. Chemosphere 289, 133170. https://doi.org/10.1016/j.chemosphere.2021.133170.

Santos, J.S., et al., 2014. Characterization of electrical discharges during spark anodization of zirconium in different electrolytes. Electrochim. Acta 130, 477–487. https://doi.org/10.1016/j.electacta.2014.03.052.

Santos, J.S., et al., 2023a. Antimicrobial properties dependence on the composition and architecture of copper-alumina coatings prepared by plasma electrolytic oxidation (PEO). Appl. Surf. Sci. 607, 155072 https://doi.org/10.1016/j.apsusc.2022.155072.

Santos, J.S., et al., 2023b. Anodized $TiO_2$ nanotubes arrays as microbial fuel cell (MFC) electrodes for wastewater treatment: an overview. J. Power Sources 564, 232872. https://doi.org/10.1016/j.jpowsour.2023.232872.

Savchuk, T.P., et al., 2022. Photocatalytic $CO_2$ conversion using anodic $TiO_2$ nanotube-$Cu_xO$ composites. Catalysts 12.

Sharma, A., et al., 2022. Insight into ZnO/carbon hybrid materials for photocatalytic reduction of CO2: an in-depth review. J. CO2 Util. 65, 102205 https://doi.org/10.1016/j.jcou.2022.102205.

Shehzad, N., et al., 2018. A critical review on $TiO_2$ based photocatalytic $CO_2$ reduction system: strategies to improve efficiency. J. CO2 Util. 26, 98–122. https://doi.org/10.1016/j.jcou.2018.04.026.

Tarek, M., et al., 2019. Hetero-structure CdS–$CuFe_2O_4$ as an efficient visible light active photocatalyst for photoelectrochemical reduction of $CO_2$ to methanol. Int. J. Hydrogen Energy 44, 26271–26284. https://doi.org/10.1016/j.ijhydene.2019.08.074.

Wang, J., et al., 2009. Structures, electronic properties, and hydrogen-storage capacity of single-walled $TiO_2$ nanotubes. Physica E: Low Dimens. Syst. Nanostruct. 41, 838–842. https://doi.org/10.1016/j.physe.2008.12.018.

Wang, T., et al., 2017. A novel and facile synthesis of black $TiO_2$ with improved visible-light photocatalytic $H_2$ generation: impact of surface modification with CTAB on morphology, structure and property. Appl. Surf. Sci. 426, 325–332. https://doi.org/10.1016/j.apsusc.2017.07.153.

Yu, L., et al., 2012. Photoelectrocatalytic performance of $TiO_2$ nanoparticles incorporated $TiO_2$ nanotube arrays. Appl. Catal., B 113–114, 318–325. https://doi.org/10.1016/j.apcatb.2011.12.004.

Zaleska, A., et al., 2008. Preparation and photocatalytic activity of boron-modified $TiO_2$ under UV and visible light. Appl. Catal., B 78, 92–100. https://doi.org/10.1016/j.apcatb.2007.09.005.

Zeng, S., et al., 2020. Optical control of selectivity of high rate $CO_2$ photoreduction via interband- or hot electron Z-scheme reaction pathways in Au-$TiO_2$ plasmonic photonic crystal photocatalyst. Appl. Catal., B 267, 118644. https://doi.org/10.1016/j.apcatb.2020.118644.

Zhang, J., et al., 2023a. Engineering defects in $TiO_2$ for the simultaneous production of hydrogen and organic products. Appl. Catal., B 333, 122765. https://doi.org/10.1016/j.apcatb.2023.122765.

Zhang, J., et al., 2021a. Interface modification of $TiO_2$ nanotubes by Biomass-derived carbon quantum dots for enhanced photocatalytic reduction of CO2. ACS Appl. Energy Mater. 4, 13120–13131. https://doi.org/10.1021/acsaem.1c02760.

Zhang, W., et al., 2023b. Mechanism of high PEC performance of B-doped TiO2 nanotube arrays: highly reactive surface defects and lattice stress. Appl. Surf. Sci. 638, 158066 https://doi.org/10.1016/j.apsusc.2023.158066.

Zhang, Z., et al., 2021b. Remarkable $CO_2$ photoreduction activity using $TiO_2$ nanotube arrays under favorable photothermal conditions driven by concentrated solar light. Appl. Phys. Lett. 119, 123906 https://doi.org/10.1063/5.0057896.

Zhao, C., et al., 2012. Ultrasonic spray pyrolysis synthesis of Ag/$TiO_2$ nanocomposite photocatalysts for simultaneous $H_2$ production and $CO_2$ reduction. Int. J. Hydrogen Energy 37, 9967–9976. https://doi.org/10.1016/j.ijhydene.2012.04.003.

Zhu, L., et al., 2018. Black $TiO_2$ nanotube arrays fabricated by electrochemical self-doping and their photoelectrochemical performance. RSC Adv. 8, 18992–19000. https://doi.org/10.1039/C8RA02983K.